Monthly Notices
of the
ROYAL ASTRONOMICAL SOCIETY

MNRAS **440,** 3317–3340 (2014) doi:10.1093/mnras/stu518

A compact, metal-rich, kpc-scale outflow in FBQS J0209−0438: detailed diagnostics from *HST*/COS extreme UV observations

Charles W. Finn,[1,2★] Simon L. Morris,[1] Neil H. M. Crighton,[3,4] Fred Hamann,[5] Chris Done,[1] Tom Theuns,[2,6] Michele Fumagalli,[7,8†] Nicolas Tejos[1,9] and Gabor Worseck[3]

[1]*Department of Physics, Durham University, South Road, Durham DH1 3LE, UK*
[2]*Institute for Computational Cosmology, Department of Physics, Durham University, South Road, Durham DH1 3LE, UK*
[3]*Max Planck Institute for Astronomy, Königstuhl 17, D-69117 Heidelberg, Germany*
[4]*Centre for Astrophysics and Supercomputing, Swinburne University of Technology, PO Box 218, Victoria 3122, Australia*
[5]*Department of Astronomy, University of Florida, 211 Bryant Space Sciences Center, Gainesville, FL 32611-2055, USA*
[6]*Department of Physics, University of Antwerp, Campus Groenenborger, Groenenborgerlaan 171, B-2020 Antwerp, Belgium*
[7]*Carnegie Observatories, 813 Santa Barbara Street, Pasadena, CA 91101, USA*
[8]*Department of Astrophysics, Princeton University, Princeton, NJ 08544-1001, USA*
[9]*Department of Astronomy and Astrophysics, UCO/Lick Observatory, University of California, 1156 High Street, Santa Cruz, CA 95064, USA*

Accepted 2014 March 13. Received 2014 February 17; in original form 2013 October 29

ABSTRACT

We present *HST*/COS observations of highly ionized absorption lines associated with a radio-loud quasar (QSO) at $z = 1.1319$. The absorption system has multiple velocity components, with an overall width of $\approx$600 km s^{-1}, tracing gas that is largely outflowing from the QSO at velocities of a few 100 km s^{-1}. There is an unprecedented range in ionization, with detections of H I, N III, N IV, N V, O IV, O IV*, O V, O VI, Ne VIII, Mg X, S V and Ar VIII. We estimate the total hydrogen number density from the column density ratio N(O IV*)/N(O IV) to be $\log(n_{\rm H}/{\rm cm}^{-3}) \sim 3$. Combined with constraints on the ionization parameter in the O IV bearing gas from photoionization equilibrium models, we derive a distance to the absorbing complex of $2.3 \lesssim R \lesssim 6.0$ kpc from the centre of the QSO. A range in ionization parameter, covering $\sim$ two orders of magnitude, suggest absorption path lengths in the range $10^{-4.5} \lesssim l_{\rm abs} \lesssim 1$ pc. In addition, the absorbing gas only partially covers the background emission from the QSO continuum, which suggests clouds with transverse sizes $l_{\rm trans} \lesssim 10^{-2.5}$ pc. Widely differing absorption path lengths, combined with covering fractions less than unity across all ions pose a challenge to models involving simple cloud geometries in associated absorption systems. These issues may be mitigated by the presence of non-equilibrium effects, which can be important in small, dynamically unstable clouds, together with the possibility of multiple gas temperatures. The dynamics and expected lifetimes of the gas clouds suggest that they do not originate from close to the active galactic nuclei, but are instead formed close to their observed location. Their inferred distance, outflow velocities and gas densities are broadly consistent with scenarios involving gas entrainment or condensations in winds driven by either supernovae, or the supermassive black hole accretion disc. In the case of the latter, the present data most likely does not trace the bulk of the outflow by mass, which could instead manifest itself as an accompanying warm absorber, detectable in X-rays.

Key words: galaxies: active – quasars: absorption lines.

1 INTRODUCTION

Associated absorption lines (AALs) seen in quasar (QSO) spectra offer a unique physical perspective on the gaseous environments in the vicinity of QSOs. Many AALs are thought to arise in

★ E-mail: c.w.finn@durham.ac.uk
† Hubble Fellow.

material that has been ejected from a region close to the super massive black hole (SMBH, within a few pc; e.g. Nestor, Hamann & Rodriguez Hidalgo 2008; Wild et al. 2008; Muzahid et al. 2012). The resulting outflows might play a major role in the quenching of star formation and in regulating the growth of SMBHs (Silk & Rees 1998; King 2003; Scannapieco & Oh 2004; Di Matteo, Springel & Hernquist 2005; Hopkins & Elvis 2010; Ostriker et al. 2010). Some may arise from material ejected in supernova explosions (e.g. Veilleux, Cecil & Bland-Hawthorn 2005). In addition, some AALs appear to probe gas that is part of the host galaxy halo (e.g. Williams et al. 1975; Sargent, Boksenberg & Young 1982; Morris et al. 1986; Tripp, Lu & Savage 1996; Hamann et al. 2001; D'Odorico et al. 2004). In some cases, this gas may eventually condense in the disc to form new generations of stars via Galactic fountain processes (Bregman 1980; Fraternali et al. 2013). The balance of gas accretion and outflow shapes the galaxy luminosity function and drives the evolution of galaxies (e.g. Benson et al. 2003; Bower et al. 2006). Observations of AALs therefore provide a detailed snapshot of these forces at work. Constraints on the metallicity of these absorbers also provide a direct measure of the star formation and chemical enrichment histories in the centres of active galaxies (Hamann & Ferland 1993, 1999).

AALs are loosely defined as having absorption redshifts within a few thousand km s^{-1} of the QSO emission redshift, and velocity widths of less than a few hundred km s^{-1}. These are narrow when compared to the so-called broad absorption lines (BALs), which have velocity widths and displacements from the QSO redshift that often exceed 10^4 km s^{-1} (Weymann et al. 1979; Foltz et al. 1986; Weymann et al. 1991; Trump et al. 2006). The origin of the BALs is presumably in a wind, driven by accretion processes close to an SMBH. However, the exact origin of the AALs is far less clear. In addition, not all AALs are necessarily intrinsic to the QSO (e.g. Tripp et al. 1996; Ganguly et al. 2013). Those that may be intrinsic show (i) absorption strength that is seen to vary on time-scales of around a year (e.g. Hamann et al. 1995; Srianand & Petitjean 2001; Hall et al. 2011; Vivek et al. 2012); (ii) metallicities $\gtrsim Z_{\odot}$ (e.g. Petitjean, Rauch & Carswell 1994; Hamann 1997; Muzahid et al. 2013); (iii) partial coverage of the QSO accretion disc continuum and/or broad-line region (BLR; e.g. Barlow & Sargent 1997; Srianand & Shankaranarayanan 1999; Gabel, Arav & Kim 2006; Arav et al. 2008); and (iv) the presence of excited fine-structure lines (e.g. Morris et al. 1986; Srianand & Petitjean 2000; Hamann et al. 2001; Edmonds et al. 2011). These properties are rarely seen in intervening absorption-line systems (see Balashev et al. 2011, for an exceptional case), and so AALs with these properties are believed to trace gas that originates near the QSO, or in the halo of the host galaxy.

AALs have been observed in optical, ultraviolet (UV) and X-ray spectra of local active galactic nuclei (AGN) and QSOs, with the X-ray observations often revealing a plethora of absorption lines and K-shell absorption edges from species with ionization potentials of a few hundred eV (e.g. O VII and O VIII). Collectively, these are usually referred to as 'warm absorbers' (in ∼50 per cent of Seyfert galaxies; Crenshaw, Kraemer & George 2003). Many authors have suggested that the presence of warm absorbers is correlated with the detection of AALs and BALs in optical and UV spectra, usually through species like C III, C IV and N V, with ionization potentials $\lesssim$100 eV (e.g. Mathur et al. 1994; Mathur, Wilkes & Elvis 1998; Brandt, Laor & Wills 2000; Kaspi et al. 2002; Arav et al. 2007; Di Gesu et al. 2013). However, at present, it is not clear whether these correlations imply a physical connection between the gas clouds traced by these ions (see, e.g., Hamann, Netzer & Shields 2000; Srianand 2000; Hamann et al. 2013).

To better understand the nature of associated absorbing clouds, more observations of the most highly ionized UV species (ionization potentials >100 eV) are required, so that the ionization structure of the absorbing gas can be more extensively characterized. At low redshift, observations of many UV ions are impossible due to the presence of Galactic Lyman-limit absorption (the relevant transitions have rest-frame wavelengths <912 Å). Observations in the optical, which are limited to high redshifts, are complicated by contamination from the Lyman α (Lyα) forest, together with a higher incidence rate of Lyman-limit systems (Fumagalli et al. 2013). At intermediate redshifts $0.5 \lesssim z \lesssim 1.5$, the problem of Galactic absorption is virtually eliminated, and the Lyα forest contamination is less severe, making this a profitable redshift range to study highly ionized AALs. Observations must be conducted in the far-ultraviolet (FUV), and with the advent of the Cosmic Origins Spectrograph (COS) on-board the *Hubble Space Telescope* (*HST*), hundreds of QSOs are now observable in this wavelength regime, thanks largely to a sensitivity more than 10 times that of the previous generation medium resolution UV spectrograph (Green et al. 2012). Together with the near-ultraviolet (NUV) modes of COS, AALs with ionization parameters of a few, to a few hundred eV are accessible. Detailed diagnostics on the ionization structure of associated gas clouds are thus available in a large number of QSOs for the first time. In addition, coverage of strong transitions due to fine-structure excited states in ions such as O IV and O V (see fig. 1 in Arav et al. 2013 for a full summary) provide powerful density diagnostics in highly ionized associated gas clouds, which provide crucial constraints on the physical conditions in and around the absorbing regions.

In this paper, we present observations of the radio-loud QSO FBQS J0209−0438 obtained with COS. This QSO was targeted as part of a larger programme of observations to study two-point correlation statistics between intergalactic medium (IGM) absorbers and galaxies at $z \lesssim 1$ (PID 12264, PI: S.L. Morris; Tejos et al. 2013). A highly ionized system of AALs is present, with complex velocity structure and an overall velocity width ≈600 km s^{-1}. We also report the detection of absorption due to the fine-structure O IV* transition. A summary of the observations and data reduction, together with a characterization of the rest-frame QSO spectral energy distribution (SED) is presented in Section 2. A complete analysis of the AALs; their covering fractions, column densities and line widths is presented in Section 3. In Section 4 we present the results of photoionization and collisional ionization models in an attempt to characterize the physical properties of the gas. In particular we examine the ionization state, metallicity and density of the gas, and use these properties to put constraints on the absorbing geometry and distance from the QSO. In Section 5 we present a discussion of these results and draw conclusions.

2 OBSERVATIONS OF FBQS J0209−0438

The QSO FBQS J0209−0438 (hereafter Q0209) was observed with *HST*/COS in 2010 December. The observations made use of both the medium-resolution ($R \sim 18\,000$) FUV and low-resolution ($R \sim 3000$) NUV modes of COS, giving wavelength coverage free from second-order light in the range 1240–3200 Å. Four central wavelength settings were used in the FUV, and three in the NUV, to ensure that the resulting spectrum had no gaps. For each central wavelength setting, multiple exposures were obtained at a number of positions offset along the dispersion direction from the

Table 1. Summary of the *HST*/COS observations.

Grating	λ_{centre} (Å)[a]	FP-POS	t_{exp} (s)[b]	x1d root name
G130M	1291	2	2321	lbj011ucq
G130M	1291	3	2948	lbj011v4q
G130M	1291	4	2948	lbj011vcq
G130M	1318	3	2948	lbj011vjq
G130M	1318	4	2948	lbj011vsq
G160M	1600	1	2276	lbj012vpq
G160M	1600	2	2948	lbj012vvq
G160M	1600	3	2948	lbj012w2q
G160M	1600	3	2948	lbj012waq
G160M	1600	4	2948	lbj012wiq
G160M	1623	1	2276	lbj013k8q
G160M	1623	2	2948	lbj013keq
G160M	1623	3	2948	lbj013kmq
G160M	1623	3	2948	lbj013ktq
G160M	1623	4	2948	lbj013l0q
G230L	2950	3	2373	lbj014vkq
G230L	2950	4	2985	lbj014vuq
G230L	2635	3	2985	lbj014w3q
G230L	3360	3	2985	lbj014wcq
G230L	3360	4	2985	lbj014wlq

[a]Central wavelength setting.
[b]Exposure time.

nominal one (FP-POS=3; see Table 1). Each offset position is separated by ∼250 pixels in the FUV channels and ∼52 pixels in the NUV channels, with FP-POS=1, 2 offset to lower wavelengths from FP-POS=3, and FP-POS=4 offset to higher wavelengths. Merging these offsets minimizes the effects of fixed-pattern noise in the COS FUV and NUV detectors by effectively dithering around these features, allowing them to be subtracted in the final co-added spectra. They are particularly crucial for the FUV modes, which suffer from additional fixed-pattern noise attributable to grid wires that produce shadows on the face of the detector. For more details, including a complete description of the design and in-flight performance of COS, see Osterman et al. (2011) and Green et al. (2012).

On 2013 October 7, under clear skies and excellent seeing conditions (∼0.55 arcsec), we obtained a near-infrared spectrum of Q0209 with FIRE (Simcoe et al. 2013), mounted on the Magellan Walter Baade 6.5 m telescope at Las Campanas Observatory. In echelle mode, and for the adopted 0.6 arcsec slit, FIRE delivers a continuous spectrum across the wavelength range 0.82−2.51 μm at a spectral resolution of ∼50 km s^{-1}. Data were collected in 2 × 729 s exposures while Q0209 was at an airmass of 1.1. To correct for spectral features arising from the Earth's atmosphere, we also acquired two spectra of the A0V star HD 25266 at similar airmass, with exposure times of 729 s each.

2.1 COS data reduction

Individual exposures from COS were downloaded from the Space Telescope Science Institute (STScI) archive and reduced using CALCOS v2.18.5. The boxcar extraction implemented in CALCOS was optimized by narrowing the source extraction box to match the apparent size of the source in the cross-dispersion direction upon inspection of each flat-fielded image. This amounted to 25 pixels for all G130M exposures, and 20 pixels for all G160M and G230L exposures. The background extraction boxes were also enlarged to encompass as much of the background signal as possible, whilst avoiding regions close to the detector edges. The CALCOS reduction procedure performs a boxcar smoothing on the background counts at each pixel along the dispersion axis to provide a robust measure of the background. This background smoothing is applied everywhere, including areas affected by scattered light from strong geocoronal emission lines, which leads to an overestimation of the background level in these regions and their immediate vicinity due to 'smearing' of the light. To avoid this, we set the background smoothing length in CALCOS to 1 pixel and perform our own background smoothing procedure in post-processing. This procedure masks out affected portions of the spectrum, namely the Lyα and O I λλ1302 + 1306 geocoronal emission lines, then interpolates across the gap to estimate the actual background level.

Alignment and co-addition procedures were performed using custom built PYTHON routines.[1] These are loosely based upon IDL routines developed by the COS GTO team.[2] They work as follows.

Individual `x1d` files (`*_x1d.fits`) produced in the CALCOS reduction are collated, along with their header information (files are listed in Section 1). Each of these files corresponds to a 1D extracted spectrum from a single central wavelength setting and FP-POS position, and contains two data extensions: an 'A' stripe and a 'B' stripe. Data quality flags[3] for all pixels are assigned new flags to mean one of three options (i) retain pixel for co-addition with a weight equal to 1, (ii) retain pixel for co-addition with a weight equal to 0.5, or (iii) discard pixel from the co-addition process. Flags assigned with option (i) are those where no anomalous condition is noted, or where unusual features have been identified in long background exposures. The latter is not expected to have any effect on the final data products except perhaps where the count rate is very low or the background higher than normal. Flags assigned with option (ii) are those in regions where the background count rate is apparently higher than the surrounding region and/or is unstable, and in regions on the FUV detector where the gain is low enough so as to affect the calibration. For the NUV channel only, regions affected by detector shadows (vignetting in this case) are assigned option (ii). These vignetted areas affect significant portions of the NUV spectrum and so are retained to avoid large gaps in the final co-added spectrum. A weight of 0.5 ensures that the data in these regions contribute significantly towards increasing the signal-to-noise ratio (SNR), whilst minimizing any additional error in the flux calibration. All other flags are assigned option (iii). Data quality flags that are assigned either of the first two options are referred to as 'good' and those assigned the latter option are referred to as 'bad.'

Next, the background counts are re-estimated, boxcar smoothing only across pixels not affected by scattered geocoronal light and with good data quality flags. The error array from CALCOS is then re-calculated with the new background smoothing lengths. These smoothing lengths are set to 1000 pixels for the FUVA stripes, 500 pixels for the FUVB stripes and 100 pixels for all NUV stripes. The numbers are arbitrary, but chosen to be large enough to ensure a robust estimation of the background, and small enough not to destroy large-scale features in the background light profile. Each spectrum is then flux calibrated using the time-dependent sensitivity curves provided by STScI, corrected to the epoch of observation.

Exposures are now co-aligned by cross-correlating regions centred on strong Galactic absorption features. Specifically, these are C II λ1334, Al II λ1670, Si II λ1260, Si II λ1526 and Mg II λλ2796, 2803. Using these features allows for co-alignment between all

[1] https://github.com/cwfinn/COS/
[2] http://casa.colorado.edu/danforth/science/cos/costools.html
[3] http://www.stsci.edu/hst/cos/pipeline/cos_dq_flags

settings in the FUV gratings (assuming the FUV wavelength scale from CALCOS is relatively correct) and between the 2635 Å and 2950 Å central wavelength settings of the G230L grating 'B' stripes. For each grating we pick the central wavelength setting and FP-POS position with the most accurately determined wavelength solutions from STScI as a reference. This is FP-POS=3 for all gratings and central wavelength settings of 1309, 1600 and 2950 Å (just the 'B' stripe) for the G130M, G160M and G230L gratings, respectively. We assume that CALCOS correctly shifts these configurations into a heliocentric reference frame. All other settings for each grating are then cross-correlated with these ones if the reference and comparison settings both contain one of the absorption features specified. Wavelength offsets are then applied to the comparison settings to match the reference ones. These offsets typically amount to a resolution element or less. For those settings that could not be aligned on any of the Galactic features specified, we searched for other strong absorption lines on which to perform the cross-correlation and found at least one absorption line for each setting. Once each exposure has been aligned, they are then scaled so that their median flux values match in overlap regions.

Before performing the final co-addition of the data, flux and error values assigned to pixels with bad data quality flags are set to zero, and pixels flagged for de-weighting have their exposure time reduced by a factor of 2. Flux and error values are then placed on a linear wavelength scale using a nearest-neighbour interpolation. The wavelength spacing is set to the dispersion of the G130M grating at $\lambda \leq 1460$ Å, the dispersion of the G160M grating at 1460 Å $< \lambda \leq 1795$ Å, and the dispersion of the G230L grating at $\lambda > 1795$ Å. Performing the interpolation in this way prior to co-addition has been shown to minimize the effects of non-Poissonian noise in the co-added data (Keeney et al. 2012). The co-addition is then performed using modified exposure-time weighting, i.e. flux values are co-added according to the following rule:

$$F_i = \frac{\sum_j F_j \times t_{\mathrm{exp};\,j}}{\sum_j t_{\mathrm{exp};\,j}}, \tag{1}$$

where i represents the ith pixel in the final, co-added spectrum and j represents the jth pixel that is co-added to make pixel i. Similarly, error values are co-added as follows:

$$\delta F_i = \frac{\sqrt{\sum_j (\delta F_j \times t_{\mathrm{exp};\,j})^2}}{\sum_j t_{\mathrm{exp};\,j}}. \tag{2}$$

Finally, the combined FUV and NUV spectra were binned to ensure Nyquist sampling, i.e. two pixels per resolution element. This corresponds to 0.0395 Å pixel^{-1} for the FUV, and a 0.436 Å pixel^{-1} for the NUV.

2.2 FIRE data reduction

Data were reduced with the FIREHOSE pipeline, which optimally extracts 1D spectra and associated errors in each order from flat-fielded 2D spectral images. The pipeline also computes the wavelength calibration using OH sky lines and ThAr arc lamp spectra obtained after each science exposure. Slit tilts in each order are measured and accounted for in the final wavelength solution, which is in vacuum and includes the heliocentric correction of 6.8 km s^{-1}. Telluric lines are corrected for in the final spectra, and each order is flux calibrated using the SPEXTOOL software package (Cushing, Vacca & Rayner 2004). Finally, the 1D spectra are optimally combined, and each order is merged in a single spectrum. The resulting SNR (order dependent) ranges between 18 and 36 per spectral pixel.

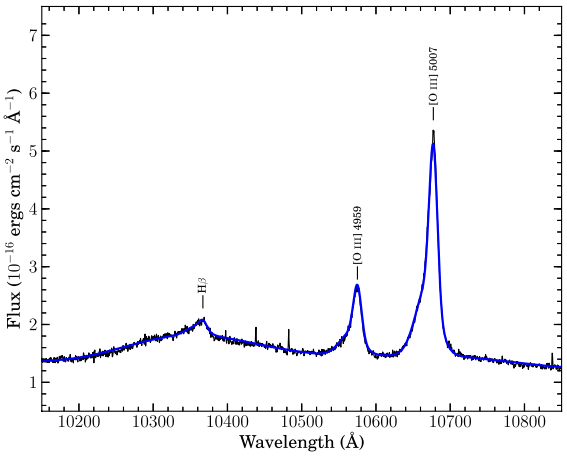

Figure 1. A region of the Magellan/FIRE spectrum of Q0209, centred on the [O III] λλ5008,4960 and Hβ emission lines. The blue curve shows the total fitted emission profile.

2.3 Redshift measurement and black hole mass

We measure the redshift of Q0209 using the [O III] λλ5008, 4960 doublet emission lines, seen in the FIRE spectrum. The region around the [O III] and Hβ emission is shown in Fig. 1. An asymmetric profile in the [O III] lines is apparent, with an extended blue wing, indicative of outflowing gas. We decompose the spectrum in this region into the contribution from a power-law continuum, blended Fe II emission lines (Gaussian smoothing over the template of Véron-Cetty, Joly & Véron 2004) and a multiple Gaussian fit to the [O III] and Hβ emission, using a similar method to that described in Jin et al. (2012). The blue curve shows the resulting best-fitting emission model. A two component Gaussian fit to each of the [O III] lines effectively removes the outflowing component. From the line centre in the stronger Gaussian component, we then derive a systemic redshift measurement of $z_{\mathrm{QSO}} = 1.131\,94 \pm 0.000\,01$, corresponding to a statistical velocity uncertainty of $\Delta v \approx 3$ km s^{-1}. The black hole mass is estimated from the full width at half-maximum (FWHM) of the broad Hβ component together with the rest-frame 5100 Å flux, using equation 3 in Woo & Urry (2002). We find a value $M_{\mathrm{BH}} \approx 1.9 \times 10^9\,\mathrm{M}_\odot$. This value compares favourably with an earlier estimation of $M_{\mathrm{BH}} \approx 1.4 \times 10^9\,\mathrm{M}_\odot$ measured from a Keck/HIRES spectrum using the broad Mg II emission line, following the method described in Matsuoka et al. (2013). The latter black hole mass estimate is used as a constraint on the accretion disc models presented in Section 2.5, which define the SED shape of Q0209 used in subsequent photoionization modelling. More details on the black hole mass estimation can be found in Done et al. (in preparation).

2.4 Continuum fitting

In order to perform a proper absorption line analysis, we require an estimate of the unabsorbed QSO continuum (including emission lines). The spectrum is then normalized using this continuum. To fit the continuum we adopted a method based on that described in Young et al. (1979), Carswell et al. (1982) and Aguirre, Schaye & Theuns (2002). The technique is as follows. First, the spectrum is split into an arbitrary number of wavelength intervals, with the flux median and standard deviation calculated in each. These intervals are chosen based on trial and error, and are on average around 12 Å wide shortward of the Lyα emission line and generally smaller

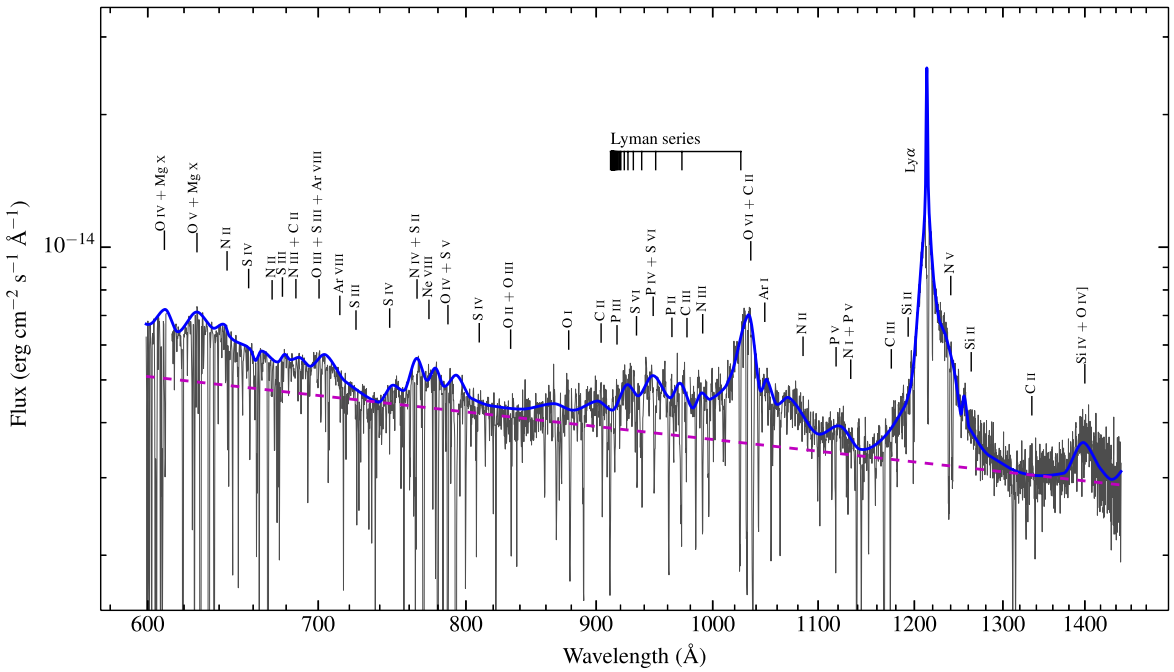

Figure 2. Rest-frame *HST*/COS spectrum of Q0209, corrected for Galactic extinction and plotted in 0.5 Å bins. The blue curve shows a spline fit to the total emission profile, as described in Section 2.4. The dashed magenta curve is a power-law fit to the continuum profile. A large number of broad emission lines are present. The expected positions of prominent broad emission lines are labelled.

across emission lines, where flux gradients vary most markedly. Larger intervals are chosen in regions free of emission lines longward of Lyα. A first-order spline is then fitted through a set of points defined by the central wavelength and median flux value in each interval. Pixels falling more than three standard deviations below the spline are rejected, then the median and standard deviation are recalculated using the remaining pixels. This process is iterated over until the remaining pixel fluxes above the spline have an approximately Gaussian distribution, with standard deviation equal to the expected 1σ flux errors. A cubic spline is then fitted to the entire spectrum to a give a smoothly varying result. Finally, the continuum has to be manually adjusted by hand in regions where the fit still appears poor, typically over strong absorption features and emission lines. The Lyα emission line strength is highly uncertain, due to strong absorption disguising the peak in the line. However, the ratio of Lyβ to Lyα line strengths in the fitted spline compares favourably with the same ratio seen in the Shull, Stevans & Danforth (2012) *HST*/COS composite spectrum of AGN, and the results of this paper are not sensitive to the exact placement of this peak.

The spline continuum is shown as a blue line on top of the rest-frame spectral data in Fig. 2, corrected for Galactic extinction using the empirical mean extinction curve of Cardelli, Clayton & Mathis (1989). We calculate the extinction as a function of wavelength using a Galactic H I column density of 2×10^{20} cm^{-2}, which sits between the measured values of 1.85×10^{20} cm^{-2} (Kalberla et al. 2005) and 2.44×10^{20} cm^{-2} (Dickey & Lockman 1990) in this direction. We assume an $E(B-V)$ to $N_{\rm H}$ ratio of 1.5 (Gorenstein 1975), which gives $E(B-V) = 0.028$. The spectrum is decomposed into the contribution from emission lines, plus that from the accretion disc continuum. We do this by choosing regions of emission line free continuum, taking the minimum value inferred from the fitted spline in each of these regions, and fitting a power law through the resulting data points, giving a spectral index of $\alpha_\lambda = -0.64$. The flux shortward of ∼600 Å (1280 Å observed frame) falls to zero due to a Lyman-limit system at $z \simeq 0.39$. A large number of broad emission lines are present, including most of the lines seen in the composite spectrum of Shull et al. (2012) over the same wavelength range. The expected locations of many prominent broad emission lines are labelled.

2.5 Spectral energy distribution

For the purposes of photoionization modelling, we construct an SED that extends from the far-infrared (∼10^{-5} keV), through to the hard X-ray bandpass (∼100 keV), which represents the range in photon energy over which most of the emission is generated by gas accretion. This emission forms the dominant contribution to the ionizing photon flux. Data points in the UV are taken from line free regions of the COS spectrum as described in Section 2.4. Optical data in the u, g, r, i and z photometric bands come from the SDSS (Ahn et al. 2013), CFHTLS (Cuillandre et al. 2012) and PanSTARRS (Chambers et al., in preparation)[4] surveys. Near-infrared data in the J, H, and $K_{\rm s}$ bands comes from 2MASS (Skrutskie et al. 2006). X-ray points are simulated from the *ROSAT* all-sky survey (Voges et al. 1999) flux and spectral index using the *ROSAT* detector response matrix.[5] The data points are corrected for Galactic dust extinction using the method described in Section 2.4, and for the Galactic absorption cross-section due to gas, grains and molecules using the model presented in Wilms, Allen & McCray (2000). We then fit the data with OPTXAGNF – an energetically self-consistent accretion disc model described fully in Done et al. (2012) – using the spectral

[4] http://www.ps1sc.org
[5] Available from http://heasarc.gsfc.nasa.gov/docs/rosat/pspc_matrices.html

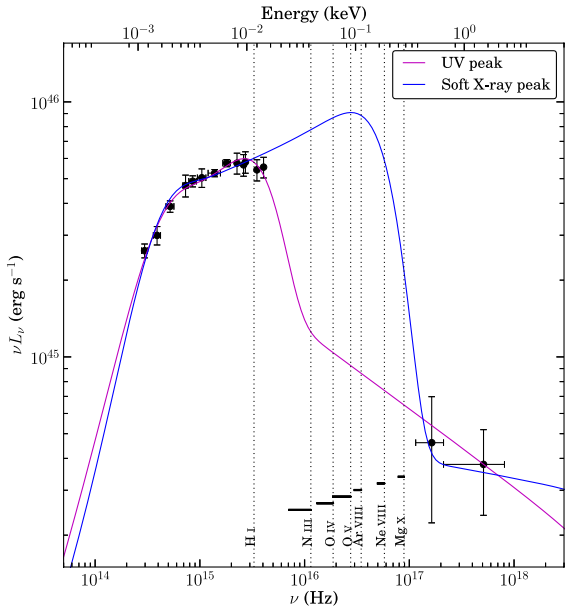

Figure 3. Rest-frame model SEDs from OPTXAGNF, fitted to extinction-corrected photometric data and line-free regions of the *HST*/COS spectrum using XSPEC. The magenta curve is the best-fitting model, which peaks in the UV. The blue curve is also a good fit to the data, but peaks in the soft X-ray bandpass. Together, these models represent the uncertainty in the SED shape over the soft X-ray region, where there is a large correction for Galactic extinction. Dotted lines represent the ionization destruction potentials for a range of ions that are used as constraints in photoionization modelling. The solid black lines represent the range of energies over which these ions are formed. Crucially, these ions are produced by photons with energies in a region where the SEDs are most markedly different, both in terms of luminosity and spectral slope.

fitting package XSPEC.[6] Briefly, the model consists of three main components: (i) a colour-temperature corrected blackbody spectrum powered by the outer regions of the black hole accretion disc, (ii) a soft X-ray excess, attributable to Compton up-scattering of seed photons in the hotter, optically thick inner region of the accretion disc, and (iii) an additional X-ray component formed through Compton up-scattering in a hot, optically thin corona above the disc, creating a power-law tail that extends through the hard X-ray bandpass. The model assumes that all the energy used to power these three components is produced through mass accretion. Therefore, the soft and hard X-ray components are physically constrained even though their origin is poorly understood. In modelling the spectrum, we assume a black hole mass of $1.4 \times 10^9\,\mathrm{M}_\odot$ (see Section 2.3). The resulting rest-frame SED is shown in Fig. 3. Two models in blue and magenta are shown that fit the data well: one peaking in the soft X-rays, the other in the UV, with normalized χ^2 values of 1.218 and 0.526, respectively. The models differ quite dramatically over the soft X-ray bandpass, representing our ignorance of the true SED shape in this region due to modelling uncertainties on the Galactic extinction across the extreme UV bandpass, and a lack of high-quality X-ray observations. Crucially, it is over this energy range where the ions considered in this paper are created (and destroyed). We therefore consider both models in later analysis. The models represent the extremes allowed by the data, and so it is useful to bear in mind that the true SED may lie somewhere between these two possibilities. The dotted vertical lines represent the ionization destruction potentials for a range of ions later considered in photoionization modelling. The solid black horizontal lines represent the range in energy where these ions are present (extending down to their ionization creation potentials).

3 ANALYSIS OF THE ASSOCIATED ABSORPTION

Sections of the COS spectrum of Q0209, together with the spline continuum (blue line) and power-law accretion disc spectrum (dashed magenta line) are shown in Fig. 4. The spectral resolutions up to, and above, 1750 Å are ∼16 and ∼100 km s^{-1} per resolution element, respectively. The plot labels just the most prominent associated absorption troughs, but we report all of the AALs detected with $>3\sigma$ significance in Table 2. Equivalent widths are measured by integrating over the whole absorption trough in each ion (including all discrete velocity components). Some of these troughs are blended with unrelated absorption lines at lower redshifts, making the measured equivalent widths larger than the intrinsic ones. We subtract away the effects of line blending by fitting Voigt profiles with VPFIT[7] (Fig. 8, Section 3.2). The velocity structure across all ions is tied to that of N IV λ765 (Fig. 5) in the fitting process, based on an empirical (by-eye) similarity between the absorption troughs. This similarity suggests that all the ions we detect in a particular velocity component are formed in regions that are co-spatial. We choose N IV λ765 as a reference, due to a lack of line blending and the fact that almost all components are cleanly resolved in this absorption trough. We have full coverage of the H I Lyman series transitions. Ions searched for, but not detected above a 3σ significance level in the AAL system are C III, O III, O V*, S III, S IV, S VI and Na IX. The expected locations of these particular lines also coincide with unrelated absorption at $z \ll z_{\mathrm{QSO}}$ in some cases.

3.1 Partial covering

In this section we look for the presence of partial covering, i.e. indications that the absorbing clouds do not fully cover the background emission from the QSO continuum and/or broad-line region (BLR). The clearest evidence for partial covering comes from flat bottomed, apparently saturated absorption troughs that do not reach zero intensity (see e.g. the O V absorption trough in Fig. 4). If the individual line components are resolved, then these profiles must be caused by optically thick absorption *plus* some unabsorbed flux. Under the assumption that the absorbers are spatially homogeneous, the residual flux at an observed wavelength λ in the normalized QSO spectrum may be written as

$$R_\lambda = (1 - C_f) + C_f \mathrm{e}^{-\tau_\lambda}, \tag{3}$$

where τ_λ is the optical depth and C_f the covering fraction, defined as the ratio of occulted to total emitted photons from the background light source(s). Solving for τ_λ we have

$$\tau_\lambda = -\ln\left(\frac{R_\lambda - 1 + C_f}{C_f}\right). \tag{4}$$

For ions with just one transition, estimating the covering fraction is only possible when the line is saturated, in which case the exponential goes to zero and $C_f = 1 - R_\lambda$. Otherwise, we cannot estimate C_f as we do not know τ_λ. However, for multiplets, where

[6] http://heasarc.nasa.gov/xanadu/xspec/

[7] http://www.ast.cam.ac.uk/rfc/vpfit.html

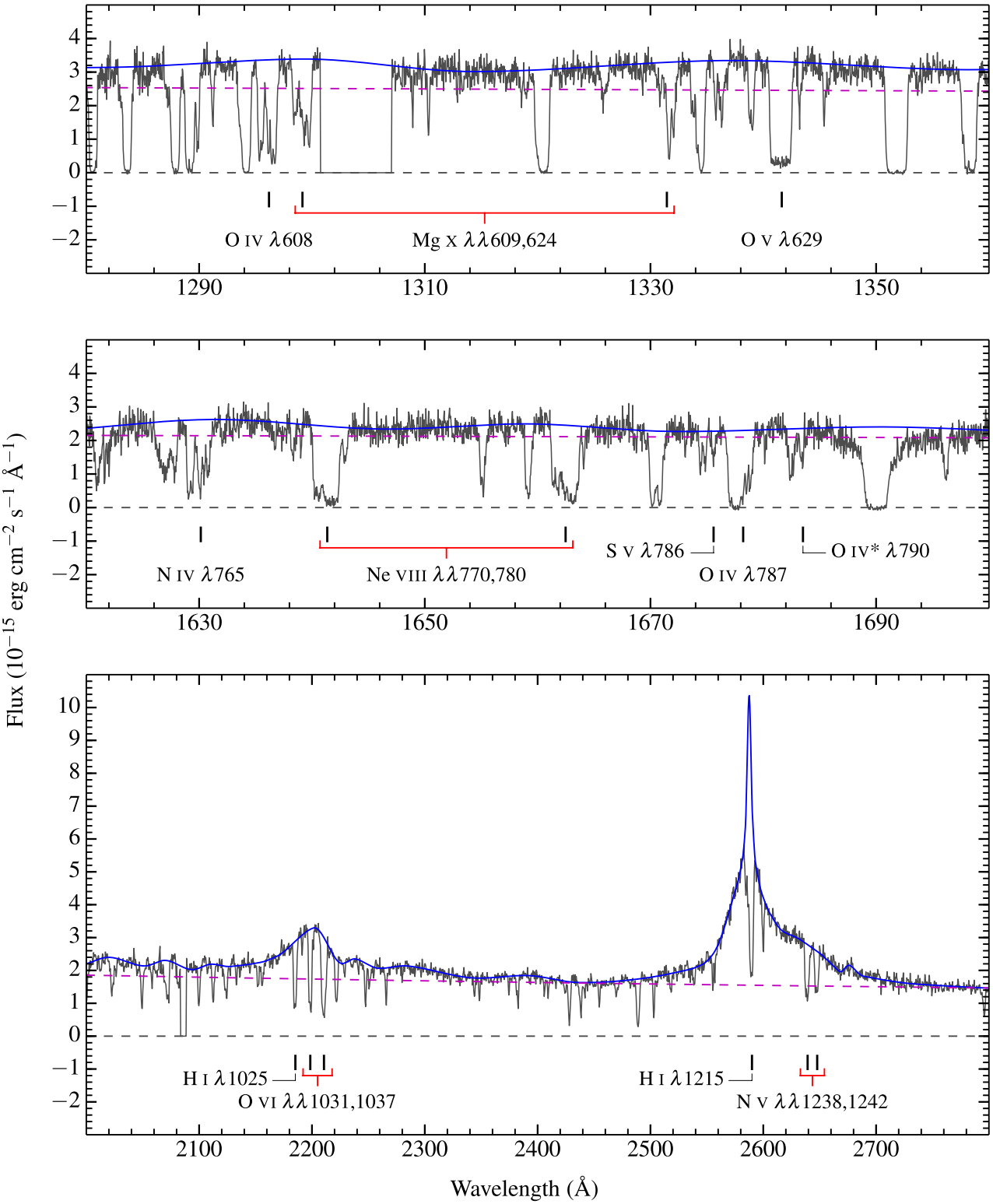

Figure 4. The *HST*/COS spectrum of Q0209 in the observed frame, shown in regions containing the most prominent AALs. The blue curve shows the unabsorbed continuum fit including emission lines. The black dashed line shows the zero-flux level. The magenta dashed line shows the power-law accretion disc continuum. Markers indicate the positions of the AALs. Labels indicate the ion (singlet or doublet) and rest-frame transition wavelengths giving rise to those absorption troughs.

Table 2. AALs detected at a $>3\sigma$ significance level, listed first in order of decreasing solar abundance relative to hydrogen, second in order of increasing ionization potential and third in order of decreasing oscillator strength.[a]

Ion	$\lambda_{\rm rest}$ (Å)[b]	IPc (eV)[c]	IPd (eV)[d]	W_λ (Å)[e]
H I	1215.7	–	13.6	2.365 ± 0.031[f]
	1025.7			1.030 ± 0.032
	972.5			0.967 ± 0.074[f]
	949.7			0.691 ± 0.045[f]
	937.8			0.757 ± 0.059[f]
O IV	787.7			0.937 ± 0.015[f]
	608.4	54.9	77.4	0.633 ± 0.008[f]
O IV*	609.8	–	–	0.362 ± 0.009[f]
	790.2			0.288 ± 0.020[g]
	790.1			0.288 ± 0.020[g]
O V	629.7	77.4	113.9	0.914 ± 0.008[f]
O VI	1031.9	113.9	138.1	1.185 ± 0.040
	1037.6			1.690 ± 0.039[f]
Ne VIII	770.4	154.2	207.3	1.072 ± 0.011[f]
	780.3			0.981 ± 0.011[f]
N III	685.0	29.6	47.4	0.126 ± 0.011[g]
	685.5			0.092 ± 0.011[g]
N IV	765.1	47.4	77.5	0.685 ± 0.014
N V	1238.8	77.5	97.9	1.076 ± 0.051
	1242.8			0.768 ± 0.054
Mg X	609.8	328.0	367.5	0.433 ± 0.008[f]
	625.0			0.362 ± 0.009[f]
S V	786.4	47.2	72.6	0.185 ± 0.015
Ar VIII	700.2	91.0	124.3	0.165 ± 0.009
	713.8			0.014 ± 0.011

[a]Atomic data from the NIST Atomic Spectra Database (http://www.nist.gov/pml/data/asd.cfm).
[b]Rest-frame transition wavelength.
[c]Ionization potential for creation.
[d]Ionization potential for destruction.
[e]Observed equivalent width across the entire absorption trough.
[f]Measured value includes a contribution from blended, unrelated absorption.
[g]Measured value includes a contribution from absorption lines due to a closely separated transition of the same ion.

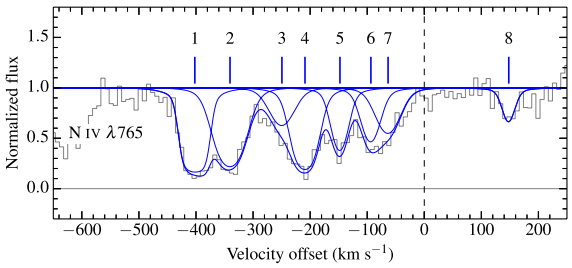

Figure 5. Velocity structure in the N IV absorption trough. Voigt components are at −402, −340, −249, −209, −148, −94, −63 and +148 km s^{-1} with respect to the QSO rest frame. The vertical dashed line marks the rest-frame velocity of the QSO. The thin blue lines are individual Voigt profile fits to the data. The thick blue line represents the overall fitted profile.

more than one transition is available, we can eliminate τ_λ by noting that

$$\gamma = \frac{\tau_{\lambda 1}}{\tau_{\lambda 2}} = \frac{f_1 \lambda_1}{f_2 \lambda_2}, \tag{5}$$

where f_1 and f_2 are the oscillator strengths of each transition. This ratio is close to 2 in the case of doublet lines. For two transitions of the same ion, with residual flux values $R_{\lambda 1}$ and $R_{\lambda 2}$, and covering fractions C_{f1} and C_{f2}, respectively, we may then write

$$R_{\lambda 1} = 1 - C_{f1} + C_{f1} \left(\frac{R_{\lambda 2} - 1 + C_{f2}}{C_{f2}} \right)^{\gamma} \tag{6}$$

(Petitjean & Srianand 1999). For simplicity we can assume that $C_{f1} = C_{f2}$ for each ion, although in general this may not be true (Srianand & Shankaranarayanan 1999). Complex velocity structure in the broad emission lines (e.g. the presence of both narrow and broad velocity components) can mean that absorbed photons from different parts of a broad-line profile will originate from spatially distinct locations (narrow-line region versus broad-line region). Unless the background emission intensity happens to be spatially homogeneous for any given wavelength, this may imply that $C_{f1} \neq C_{f2}$, even for doublets that have a relatively small wavelength separation (see e.g. the O VI doublet in Fig. 4, which spans the centre and the blue wing of the Lyβ + O VI emission line). In addition, over the whole wavelength range of the QSO spectrum, there are regions dominated more by the accretion disc continuum than by the BLR, and vice versa. Since the BLR is larger in size than the continuum, if the absorbing clouds have transverse sizes larger than the continuum region, this can also lead to an inequality. We expect deviations from $C_{f1} = C_{f2}$ to be small in most cases, although the relatively high Lyα emission line flux can lead to situations where the Lyα absorption profile has a smaller apparent optical depth than the Lyβ profile (e.g. Petitjean & Srianand 1999). Nevertheless, we do not see strong evidence for this effect in our data, and therefore we favour a scenario where there are many clouds with transverse sizes smaller than the continuum size ($\lesssim$4 light-days; Jimenez-Vicente et al. 2012). In what follows, we assume $C_{f1} = C_{f2}$ within the measurement uncertainties.

Residual flux is clearly present in the saturated absorption troughs of O V λ629 and Ne VIII λ770 (at the blue end), which implies that $C_f < 1$ for these ions (see Fig. 4). Taking the average normalized residual flux across the flat portions of these profiles gives covering fractions of 0.91 ± 0.01 and 0.93 ± 0.01, respectively (with $\tau \gg 1$ in equation 3). In these, and all following covering fraction estimates, the quoted statistical error does not include any contribution from the error on the continuum fit. We also caution that the error bars assume Gaussian statistics, which underestimate the true flux error in absorption troughs where the number of counts in a given bin is low ($\lesssim$100; Gehrels 1986). Given the flat profile across the entirety of the O V absorption trough, there is no strong evidence for covering fractions that change across the profiles. We can check this further by examining the apparent doublet ratio for Ne VIII in components that are unsaturated, and unaffected by blending with unrelated absorption lines. There is one component where this measurement is possible in the case of Ne VIII. Covering fractions can also be determined in this way for Mg X and O IV. The former has one velocity component available that meets the aforementioned criteria, and the latter has one that is still mildly affected by line blending. We first calculate the apparent optical depth as a function of velocity across the stronger transition for each ion, then scale these optical depths by γ (equation 5) to predict the optical depths in the weaker transitions. The difference between the observed and predicted profiles for the weaker member of each ion can be seen in Fig. 6. The dashed blue lines show the velocity centroids of the components used to measure the covering fractions. We determine covering fractions by numerically solving Fig. 6 over a ∼40 km s^{-1} region centred on each velocity component (blue shaded regions in Fig. 6), and average the results. This procedure gives covering fractions of 0.92 ± 0.08 for O IV, 0.84 ± 0.10 for Ne VIII, and 0.74

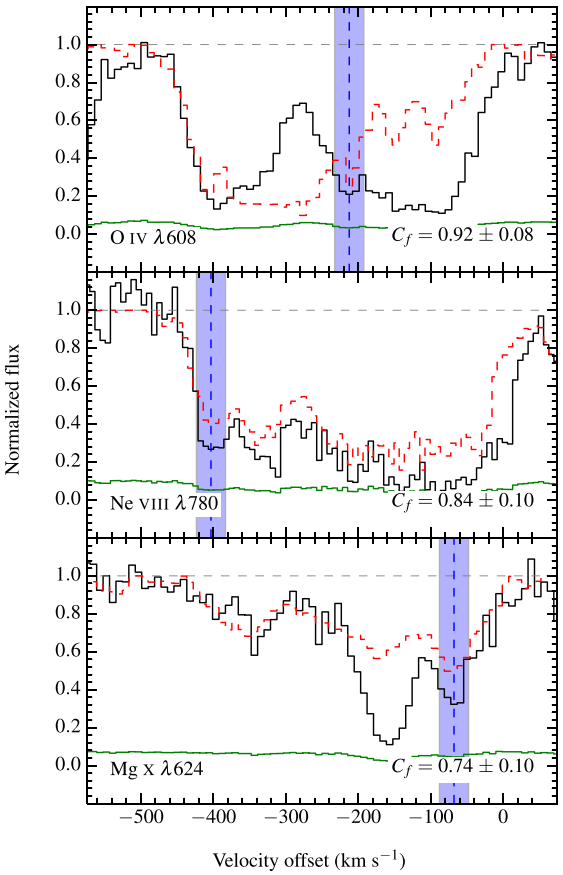

Figure 6. Observed (solid black line) compared to predicted (dashed red line) profiles of O IV λ608, Ne VIII λ780 and Mg X λ624 based on apparent optical depth measurements of their stronger counterparts, O IV λ787, Ne X λ770 and Mg X λ609, respectively. The deeper observed compared to predicted profiles indicate partial covering of the background emission. This situation is occasionally inverted due to line blending. The velocity offset is with respect to the QSO rest frame. The green line is the 1σ error on the normalized flux in each pixel. The dashed blue lines represent the velocity centroids of the lines not affected (or minimally affected) by blends from unrelated absorption. Vertical shaded regions represent the range of velocities over which covering fractions are calculated (per pixel). Quoted C_f values are the average of those calculated within these regions.

$\pm$ 0.10 for Mg X. For O IV, we note that the chosen velocity component is mildly affected by blending, which may add an additional uncertainty on top of the measured one. We also note that the Ne VIII covering fraction determined from this method is consistent with that measured from the saturated blue wing of Ne VIII λ770 within the 1σ uncertainty, and adopt the latter result as the covering fraction for this ion.

For O IV* λλ609, 790 we first note that one of these transitions overlaps with that of Mg X λ609. Therefore, to determine the covering fraction, we first perform a fit to the Mg X λ624 absorption trough, taking into account the covering fraction already determined for this ion, and fixing the velocity structure to that from the fit to N IV λ765 (Fig. 5). We then re-normalize the spectrum using the calculated Mg X profile, leaving just the absorption signature from O IV*. It is subsequently apparent that the covering fraction for O IV* is consistent with that of O IV. We do not attempt to explicitly calculate the covering fraction in this case, due to the additional uncertainty imposed by subtracting the Mg X absorption. Examining multiplet ratios in N III and Ar VIII reveals that these ions are

Table 3. Adopted covering fractions.

Ion	Measurement[a]	C_f[b]	ΔC_f[c]
H I	Inferred	0.92	–
N III	Inferred	0.92	–
N IV	Inferred	0.92	–
N V	Inferred	0.91	–
O IV	Direct	0.92	0.08
O IV*	Inferred	0.92	–
O V	Direct	0.91	0.01
O VI	Inferred	0.91	–
Ne VIII	Direct	0.93	0.01
Mg X	Direct	0.74	0.10
S V	Inferred	0.91	–
Ar VIII	Inferred	0.91	–

[a]Measurements are either direct (based on saturated lines or from comparing line ratios) or inferred (assumed to be the same as that measured directly from an ion with similar ionization potential).
[b]Assuming the covering fraction of the continuum is the same as the covering fraction of the BLR. Requires many clouds smaller than the size of the continuum region.
[c]1σ statistical uncertainty on the covering fraction (for directly measured values only, not including errors on the continuum fit).

consistent with a covering fraction of unity, however their detection significance is considerably smaller than for the rest of the ions detected here. Therefore C_f may still be less than 1, as found for ions with better measurements.

For the remaining AALs, covering fractions are even more difficult to determine. In the case of N IV and S V, it is because they are singlet ions (only one transition). In all other cases it is because the lines fall in the NUV portion of the spectrum, where the lower resolution complicates the process of determining the true residual flux in each line (since individual components are not resolved). The relative contributions of partial covering fractions and resolution effects to the line ratios are very difficult (or impossible) to disentangle. For these lines, the simplest approach is to take another ion with measured covering fraction that is assumed to trace the same gas, and adopt this covering fraction. We deem the best (available) choice of ion, for which this assumption might hold, to be that with the most similar ionization potential. We adopt this approach also in the case of N III and Ar VIII. Matching ions under this criterion gives two groups: (O IV, H I, N III, N IV, S V) and (O V, N V, O VI, Ar VIII), where only the first member of each group has a measured covering fraction. Covering fractions for all ions are summarized in Table 3. Despite the uncertainties in assigning covering fractions for the absorption lines in our sample, we note that all measured values are high ($C_f \sim 0.9$) with the possible exception of Mg X, and produce statistically good results in Voigt profile fitting (Section 3.2). In general, we find that the results of this paper are not sensitive to the precise values of the covering fractions. Indeed, if we take the best measured covering fraction from O V and apply this to all ions, the results we obtain are largely consistent with those obtained later, within the measurement uncertainties.

3.2 Column densities and line widths

To measure the column densities for each ion, we first perform a simultaneous Voigt profile fit to all of the AALs in the medium resolution, FUV part of the spectrum, using VPFIT. We do so with the assumption that all ions must share the same eight separate velocity components, this number having been determined from an independent fit to the N IV λ756 absorption trough (see Section 3.1).

Table 4. Column density and Doppler broadening parameter measurements of the AALs.

Ion	v_1	v_2	v_3	v_4	v_5	v_6	v_7	v_8
				$\log(N/\mathrm{cm}^{-2})$				
H I	14.64 ± 0.32	14.99 ± 0.41	14.92 ± 0.65	14.97 ± 0.97	14.94 ± 0.97	14.83 ± 0.77	14.50 ± 0.29	<13.46
N III	<12.99	<12.99	<12.99	13.41 ± 0.09	<12.99	<12.99	<12.99	<12.99
N IV	>14.11	14.03 ± 0.05	13.42 ± 0.26	14.09 ± 0.11	13.61 ± 0.07	13.50 ± 0.11	13.49 ± 0.10	13.08 ± 0.14
N V	13.83 ± 0.93	>13.89	>13.86	>13.93	>13.95	>13.90	>13.83	<14.06
O IV	>14.74	15.02 ± 0.04	14.54 ± 0.22	14.93 ± 0.14	14.59 ± 0.11	14.51 ± 0.09	14.12 ± 0.15	13.68 ± 0.12
O IV*	14.45 ± 0.06	14.10 ± 0.12	<13.46	14.22 ± 0.07	<13.46	<13.46	<13.46	<13.46
O V	>14.24	>14.34	>14.39	>14.24	>14.14	>14.22	>14.22	13.62 ± 0.09
O VI	>13.90	>14.21	>14.22	>14.25	>14.34	>14.35	>14.28	<14.12
Ne VIII	14.94 ± 0.07	14.91 ± 0.19	15.06 ± 0.29	15.10 ± 0.15	>14.83	>15.01	>14.91	<13.48
Mg X	<13.46	14.50 ± 0.12	14.80 ± 0.28	14.68 ± 0.39	14.78 ± 0.19	14.54 ± 0.54	15.29 ± 0.09	<13.46
S V	13.14 ± 0.07	12.97 ± 0.08	<12.40	12.90 ± 0.09	<12.40	<12.40	<12.40	<12.40
Ar VIII	13.19 ± 0.13	13.28 ± 0.13	<12.82	13.34 ± 0.09	<12.82	13.26 ± 0.22	13.04 ± 0.29	<12.82
				$b\ (\mathrm{km\ s}^{-1})$				
H I	24	34	35	29	26	28	33	–
N III	–	–	–	34 ± 12	–	–	–	–
N IV	–	27 ± 3	27 ± 13	20 ± 3	15 ± 4	18 ± 6	25 ± 6	10 ± 7
N V	18 ± 106	–	–	–	–	–	–	–
O IV	–	26	27	20	15	18	25	10
O IV*	20 ± 4	33 ± 14	–	17 ± 6	–	–	–	–
O V	–	–	–	–	–	–	–	13 ± 5
O VI	–	–	–	–	–	–	–	–
Ne VIII	19 ± 2	26 ± 7	77 ± 76	29 ± 12	–	–	–	–
Mg X	–	14 ± 6	171 ± 78	54 ± 33	31 ± 12	109 ± 96	25 ± 5	–
S V	18 ± 5	17 ± 6	–	23 ± 8	–	–	–	–
Ar VIII	16 ± 9	41 ± 19	–	25 ± 9	–	49 ± 22	22 ± 19	–

Voigt profiles are convolved with the wavelength dependent, non-Gaussian COS line spread function (LSF). We calculate the LSF at the observed wavelength of each transition by interpolating between the tabulated LSFs, which are specified at a discrete set of wavelengths (Ghavamian et al. 2009; Kriss 2011).

For the remaining ions in the low resolution, NUV part of the spectrum, individual components are not resolved, and so these data give very poor constraints on the Doppler broadening (b) parameters, which adds to the uncertainty on the column densities. Crucially, coverage of the H I Lyman series absorption, for which we require well-constrained column densities in forthcoming photoionization analysis, is limited to the NUV spectrum. One way of reducing this uncertainty is to find pairs of ions that likely trace the same gas, then require that the b values for these pairs follow some scaling relation, thus reducing the number of degrees of freedom in the χ^2 minimization. Tying b values sensibly requires knowledge about both the thermal and turbulent motions in the gas. We define b as

$$b^2 = b_{\mathrm{turb}}^2 + \frac{2kT}{m}, \tag{7}$$

where b_{turb} is the turbulent contribution to the line width, k is Boltzmann's constant, T is the gas temperature and m is the atomic mass of the ion in question. The relationship between b values in two ions, labelled b_1 and b_2, can then be expressed as

$$b_1^2 = \left(\frac{m_2}{m_1}\right) b_2^2 + b_{\mathrm{turb}}^2 \left(1 - \frac{m_2}{m_1}\right). \tag{8}$$

If b_{turb} is zero, then b values can be related by a simple mass scaling. We note that if the gas is photoionized, with a nominal temperature $T \sim 10^4$ K, then initial fits to the FUV data indicate that

$$b_{\mathrm{turb}} = \sqrt{b^2 - \frac{2kT}{m}} > 0 \tag{9}$$

(see Table 4). In fact, for $T < 10^5$ K, turbulence dominates the broadening for these lines given the measured b values. Therefore, if the gas is photoionized, we cannot relate b values by the masses of the ions alone.

We can try to determine a plausible range in T by choosing two ions that are assumed to trace the same gas, and whose individual components would then likely possess the same b_{turb}. We note that O IV and N IV have almost identical ionization destruction potentials, and very similar ionization creation potentials (54.9 and 47.4 eV, respectively), making it likely that these ions will satisfy this criterion. We can then require that b_{turb} be the same for each, such that

$$b(\mathrm{N\,IV}) = \sqrt{b^2(\mathrm{O\,IV}) + 2kT\left(\frac{1}{m(\mathrm{N})} - \frac{1}{m(\mathrm{O})}\right)}. \tag{10}$$

We proceed by fitting Voigt profiles to O IV and N IV, requiring that these ions share the same eight velocity components as before, but additionally force the b values to scale as in equation (10), for a range of temperatures between $\sim 10^4$ and $\sim 10^6$ K. The resulting normalized χ^2 values on the fit as a function of gas temperature are shown as the black curve in Fig. 7. Above temperatures of $\sim 10^{5.5}$ K, normalized χ^2 values on the fit start to increase dramatically, and we conclude that the data favour gas temperatures less than this value. Turbulence dominates the line broadening at these temperatures, and so scaling b values between pairs of ions based on their masses alone will not be sufficient. Green and red dotted curves in Fig. 7

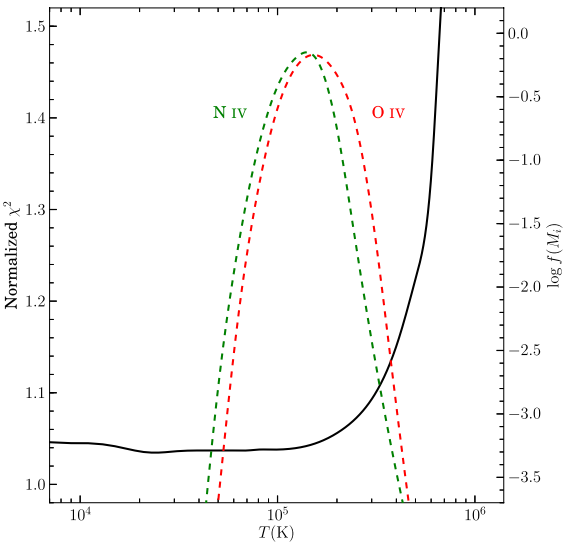

Figure 7. Normalized χ^2 values for Voigt profile fits to the N IV and O IV absorption troughs as a function of temperature, assuming their b values scale as in equation (10). The normalized χ^2 value is minimized in the range $10^4 \lesssim T \lesssim 10^5$ K; temperatures characteristic of photoionized gas. Green and red dotted curves show, for CIE, the predicted ion fractions of N IV and O IV, respectively, as a function of temperature. Both peak at $\sim 10^5$ K, and we are therefore not able to rule out the possibility that the gas is collisionally ionized.

show, in the case of a collisionally ionized medium, the expected ion fractions of N IV and O IV, respectively, as a function of temperature (Mazzotta et al. 1998). Both ion fractions peak at $\sim 10^5$ K, and we are therefore not able to rule out the possibility that the gas is in collisional ionization equilibrium (CIE) based on line widths alone.

We proceed by assuming the gas traced by N IV and O IV has a characteristic temperature of 3×10^4 K (a reasonable value based on Fig. 7) and use this information to constrain the b values in H I. This procedure minimizes the uncertainty in the H I column densities, crucial for later photoionization modelling. We first assume that $b_{\rm turb}$ for N IV be roughly the same as that for O IV and H I, then apply a b scaling between these ions like that in equation (10). The assumption that N IV and O IV trace the same gas is already well motivated based on the similarity in their ionization potentials. To extend this argument to H I, with ionization potential >5 times smaller than these ions, we assume that most of the H I is locked up in the same gas as traced by N IV and O IV. We note that this assumption is justified later in Section 4 upon consideration of the measured column densities and the ionization fractions derived from photoionization models. It is reassuring to note that the column density measurements resulting from this approach are insensitive to the assumed temperature over the range $10^4 \lesssim T \lesssim 10^5$ K, where the normalized χ^2 values in Fig. 7 are minimized. Therefore, the gas temperature we assume in the O IV/N IV gas is (nearly) independent of any constraints later obtained in Section 4.

All ions are now fitted simultaneously, tying the velocity structure to the eight components identified in N IV (Fig. 5) as before, but with an additional b scaling between N IV, O IV and H I as described. All other b values are allowed to float. The resulting fit has a normalized χ^2 value of 1.37 and is shown in Fig. 8. Transitions are ordered first by atomic mass, and second by oscillator strength. The dashed vertical line indicates the rest-frame velocity of the QSO. Individual blue Voigt profiles represent those components attributable to the labelled ion and transition, whereas red profiles represent components from unrelated blended transitions. Most of these blends are constrained by accompanying transitions of the same ion. The two most prominent blends with O IV λ608 and the blend with Mg X λ625 at $\sim$400 km s^{-1}, are assumed to be H I Lyα. The thick blue line represents the overall model absorption trough, and the green points show the residuals on the fit, with the solid black lines marking the $\pm 1\sigma$ standard deviation. Line saturation is evident from the Lyα absorption trough, although we note that the column densities are well measured due to a large number of observed transitions in the H I Lyman series.

Column densities and Doppler broadening parameters are listed on a component by component basis (v_1–v_8, ascending in velocity offset), together with their 1σ error bars in Section 4. For components where no absorption line is detected in any given ion, we calculate the upper bound on the equivalent width at the 3σ significance level, derived using equations (4)–(5), (7) and (9)–(10) in Keeney et al. (2012), then perform the conversion to column density assuming a linear curve of growth. For column densities with 1σ uncertainties greater than 1 (typically when $\tau \gg 1$, i.e. where the lines are saturated), we quote lower limits on the column densities, based on the apparent optical depth at the line centres (calculated using equation 4) and assuming a b value of 25 km s^{-1}, which is approximately typical of the well-measured lines. We do not list b values for components that have upper or lower limits on the column densities. Error bars are not presented for inferred b values.

4 PROPERTIES OF THE ASSOCIATED ABSORBERS

In the following section, we first present constraints on the electron number density in the clouds based on an analysis of the fine-structure transition O IV*. We then consider both photoionization and CIE models, and use these to put constraints on the properties of the associated gas clouds. Models are generated using version c13.00 of CLOUDY, described in Ferland et al. (2013). We note that, in general, absorbers may not be in ionization equilibrium (e.g. Oppenheimer & Schaye 2013a,b). This possibility is discussed later in Section 5.2.

4.1 Electron number density in the absorbing clouds

In this section we present analysis on the absorption due to fine-structure, metastable transitions in O IV, which enables us to estimate the electron number density in the clouds giving rise to the absorption by O IV. First, we note that O IV* arises from doublet fine structure ($J = 1/2$ and $3/2$) in the ground state, which should behave approximately as a two-level atom, where the level populations are controlled by collisional processes and forbidden radiative decays (Bahcall & Wolf 1968). If we neglect stimulated emission, the only acting processes are collisional excitation, collisional de-excitation and radiative decay. The energy level spacing corresponds to 25.91 μm, or 1.2×10^{13} Hz, so we find this to be a fair approximation on the basis of Fig. 3, together with the fact that stimulated emission is extremely forbidden. We denote the ground state as level 0, the excited state as level 1, and let n_j be the number density (cm^{-3}) of O IV in level j. If we assume that collisional excitation is dominated by electrons, then the population of the excited state must satisfy

$$\frac{{\rm d}n_1}{{\rm d}t} = n_{\rm e} n_0 k_{01} - n_{\rm e} n_1 k_{10} - n_1 A_{10} \qquad (11)$$

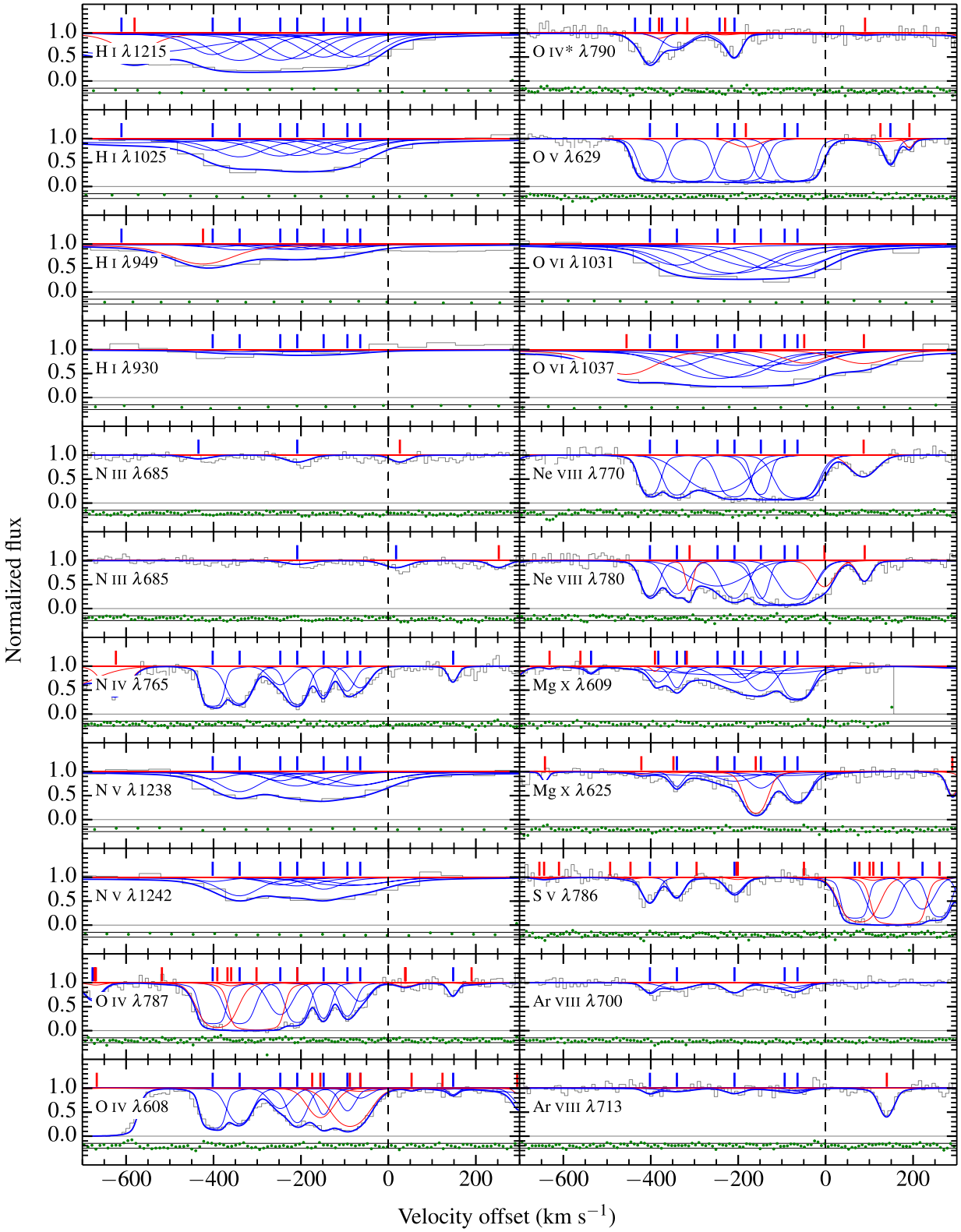

Figure 8. Voigt profiles fitted to the AALs in the *HST*/COS spectrum of Q0209. Thin blue lines are the individual velocity components for each labelled ion. Thin red lines are the blended components. The thick blue line in each panel is the total summed profile. The dashed line represents the rest-frame velocity of the QSO. The green points are the residuals between the model and the data, with the solid black lines representing the $\pm 1\sigma$ standard deviation.

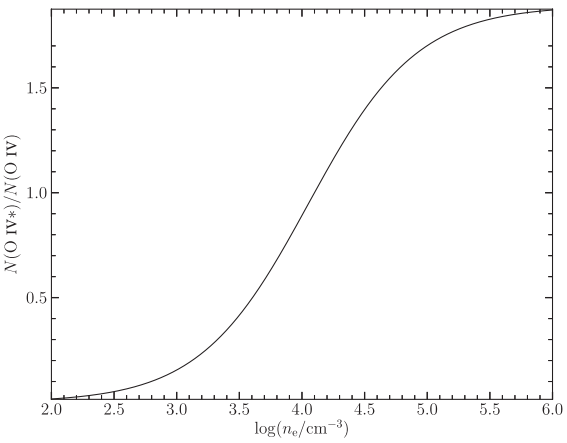

Figure 9. The electron number density n_e as a function of the column density ratio between O IV* and O IV based on predictions from a theoretical level population assuming a temperature of 10^4 K.

(Draine 2011), where n_e is the electron number density (cm^{-3}), k_{01} and k_{10} are the upward and downward rate coefficients (cm^3 s^{-1}), respectively, and A_{10} is the spontaneous decay rate (s^{-1}). For a steady state ($dn_1/dt = 0$), we then require

$$\frac{N(\mathrm{O\,IV}^*)}{N(\mathrm{O\,IV})} = \frac{n_e k_{01}}{n_e k_{10} + A_{10}}, \tag{12}$$

where we have now replaced the number densities by the observed column densities. We can write k_{01} in terms of k_{10} as follows:

$$k_{01} = \frac{g_1}{g_0} k_{10} e^{-E_{10}/kT}, \tag{13}$$

where g_0 and g_1 are the level degeneracies, E_{10} is the energy level difference and T is the kinetic temperature of the gas. We can additionally define the critical electron density, at which the collisional de-excitation rate equals the radiative de-excitation rate:

$$n_{\mathrm{crit}} \equiv \frac{A_{10}}{k_{10}}. \tag{14}$$

The electron number density can then be written as

$$n_e = n_{\mathrm{crit}} \left(\frac{N(\mathrm{O\,IV})}{N(\mathrm{O\,IV}^*)} \frac{k_{01}}{k_{10}} - 1 \right)^{-1}. \tag{15}$$

Assuming a temperature of 10^4 K, we can write

$$k_{10} = 8.629 \times 10^{-8} \frac{\Omega_{10}}{g_1}\ \mathrm{cm^3\ s^{-1}}, \tag{16}$$

where Ω_{10} is the collision strength connecting levels 1 and 0. For electrons at this temperature, the collision strength is $\Omega_{10} = 2.144$ (Tayal 2006). We take $A_{10} = 5.19 \times 10^{-4}$ s^{-1} from the NIST atomic spectra data base.[8] The resulting dependence of n_e on the ratio $N(\mathrm{O\,IV}^*)/N(\mathrm{O\,IV})$ is shown in Fig. 9. Comparing to fig. 12 in Arav et al. (2013), we find an excellent agreement. For a highly ionized plasma, assuming solar metallicity and abundances, we can relate n_e to the hydrogen number density n_H as

$$n_e = n_H \left(1 + 2\frac{n_{\mathrm{He}}}{n_H} + \sum_{i \geq 3} Z_i \frac{n_{Z_i}}{n_H} \right) \approx \frac{1+X}{2X} n_H, \tag{17}$$

where Z_i is the atomic number of element i and X is the mass fraction in hydrogen. For a value $X = 0.71$ we have $n_e \simeq 1.2 n_H$. We

[8] http://www.nist.gov/pml/data/asd.cfm

Table 5. Total hydrogen number density in each velocity component.

log (n_H/cm^{-3})							
v_1	v_2	v_3	v_4	v_5	v_6	v_7	v_8
$\lesssim$3.54	2.80 ± 0.13	$\lesssim$2.63	3.03 ± 0.17	$\lesssim$2.70	$\lesssim$2.66	$\lesssim$3.09	$\lesssim$3.64

calculate n_H in the gas traced by O IV for each velocity component using equation (15), and summarize the results in Table 5. Where there is a lower limit on the O IV column density, or an upper limit on the O IV* density, this results in an upper limit on n_H. We caution that these upper limits are only approximate, as they are sensitive to the adopted significance level used to calculate limiting equivalent widths, and the assumed b value used to calculate the lower limit on the O IV column density. We find that a value $\log(n_H/\mathrm{cm^{-3}}) \sim 3$ is representative for the AAL region as a whole.

4.2 Photoionization analysis

In the following we assume that the gas clouds are in photoionization equilibrium with either of the QSO SEDs determined in Section 2.5. The two main parameters that best describe the photoionization structure are the total hydrogen column density (N_H) and the ionization parameter (U). The latter is defined as the dimensionless ratio between the number density of hydrogen atoms and the number density of photons that ionize hydrogen at the illuminated face of the absorbing gas clouds. We express this as

$$U \equiv \frac{1}{4\pi c R^2 n_H} \int_{\nu_{LL}}^{\infty} \frac{L_\nu}{h\nu} d\nu, \tag{18}$$

where ν is the frequency, c is the speed of light, L_ν is the luminosity density of the QSO (erg s^{-1} cm^{-2} Hz^{-1}), ν_{LL} is the frequency corresponding to the Lyman limit (912 Å), R is the radial distance between the absorber and the QSO and n_H is the total hydrogen density (i.e. H I + H II). The equations of ionization and thermal balance are then solved using CLOUDY. We run the code multiple times to form 3D grids of predicted quantities over (U, N_H, Z) parameter space, where Z is the metallicity of the gas, normalized to solar metallicity. We vary the parameters U and N_H in steps of 0.1 dex, and Z in steps of 1 dex, assuming a constant total hydrogen density. The results from these grids are the subject of this section and Section 4.4.

Shown in Fig. 10 are theoretical ionization fractions of H I and various metal ions for which we have reliable column density estimates as a function of U. We show model curves for clouds in photoionization equilibrium with both the 'UV peak' and 'Soft X-ray peak' SEDs (see Section 2.5). These results are not sensitive to the abundances used in the calculations (in this case we have used solar abundances), and neither are they sensitive to the total column densities. This is because the model clouds are optically thin in the Lyman continuum, which means that there are no steep gradients in ionization (e.g. due to shielding from an H II–H I recombination front). We note that this situation is a good approximation to the real one, given the absence of absorption at the Lyman limit. We calculate the column density ratios $N(\mathrm{O\,IV})/N(\mathrm{O\,V})$ and $N(\mathrm{Ne\,VIII})/N(\mathrm{Mg\,X})$ in the components where those ratios are best measured, then find the range in ionization parameter over which each is predicted within their 1σ uncertainties. For $N(\mathrm{Ne\,VIII})/N(\mathrm{Mg\,X})$ we scale by relative solar abundances. The resulting constraints on U are plotted as a series of vertical bars.

From Fig. 10 it is clear that the gas has a range in ionization parameter that covers around two orders of magnitude. At a fixed

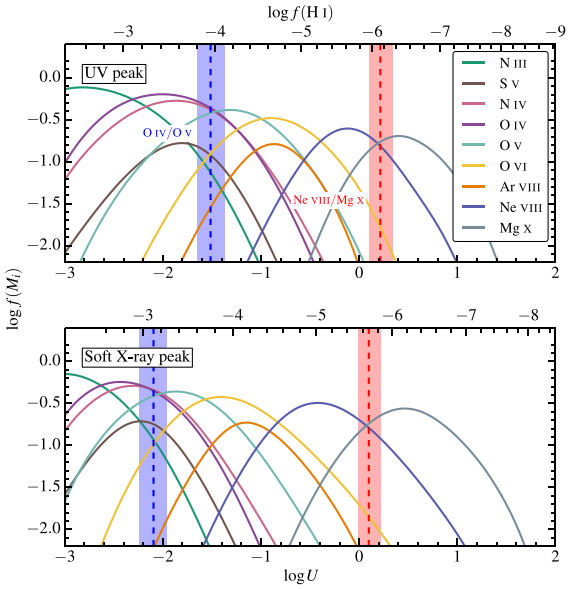

Figure 10. Theoretical ionization fractions for a range of metal ions $f(M_i)$ in optically thin clouds in photoionization equilibrium with the 'UV peak' SED (top panel) and the 'Soft X-ray peak' SED (bottom panel), plotted as a function of ionization parameter. Curves are colour coded by ion. The H I fraction is shown on the top axis. The vertical bars indicate the range in ionization parameter allowed for by measured column density ratios in components where those ratios are best measured. For N(Ne VIII)/N(Mg X) we scale by relative solar abundances. These ratios indicate there is a range in ionization parameter covering nearly two orders of magnitude under photoionization equilibrium.

distance R from the QSO, this corresponds to a range in gas density that covers around two orders of magnitude. Measuring the same column density ratios in different velocity components to those plotted (including column density lower limits) gives constraints on the ionization parameters that are fully consistent with those obtained above. This range of ionization parameter is therefore representative for the AAL region as a whole.

4.3 Collisional ionization equilibrium

We next consider a situation whereby the AAL clouds are in CIE. To simulate CIE, we run CLOUDY multiple times with $\log U = -5$ (so that the effect of the radiative field is negligible), holding temperature constant for values in the range $4.5 \leq T \leq 6.5$. Shown in Fig. 11 are theoretical ionization fractions of various metal ions for which we have reliable column density estimates under CIE as a function of temperature. Like Fig. 10, the results are not sensitive to the specific abundances adopted, or the total column density. Vertical bars indicate the range in temperature permitted according to the best-measured column density ratios N(O IV)/N(O V) and N(Ne VIII)/N(Mg X) within their 1σ uncertainties. Again, for N(Ne VIII)/N(Mg X) we scale by relative solar abundances. It is clear that temperatures cover more than an order of magnitude in the AAL region if the gas is in CIE. Similarly to the case of photoionization, constraints on the temperature are consistent between different velocity components.

To determine whether CIE is allowed by the data, we model clouds illuminated by the 'UV peak' incident continuum, assuming an H I column density of 10^{15} cm^{-2} (matching the observed value in velocity component v_2), a total hydrogen density of

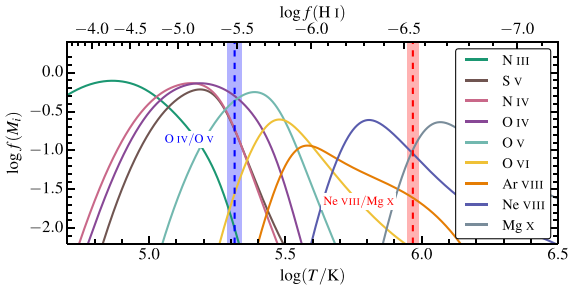

Figure 11. Theoretical ionization fractions for a range of metal ions $f(M_i)$ under CIE as a function of temperature. Curves are colour coded by ion. The vertical bars indicate the range in temperature allowed for by measured column density ratios in components where those ratios are best measured. For N(Ne VIII)/N(Mg X) we scale by relative solar abundances. These ratios indicate a range covering more than an order of magnitude in gas temperature under CIE.

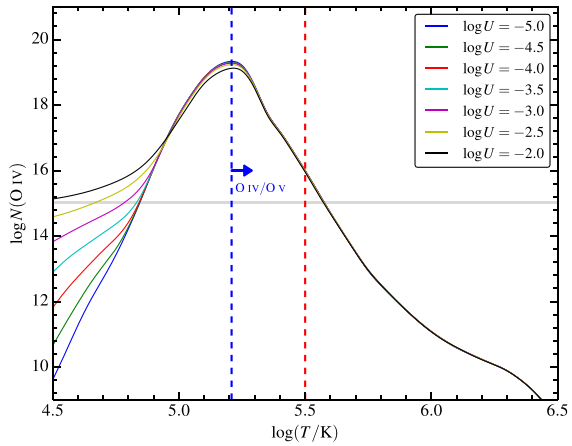

Figure 12. The predicted O IV column density as a function of gas temperature for a range of ionization parameters and a fixed H I column density of 10^{15} cm^{-2}. The dashed blue vertical line and accompanying arrow denotes a lower limit on the temperature of the gas clouds giving rise to the majority of the O IV absorption under CIE, inferred from the ratio N(O IV)/N(O V). The vertical red dashed line marks the maximum temperature allowed from an analysis of the absorption line widths. The horizontal grey shaded bar represents the 1σ constraints on the O IV column density from velocity component v_2. Theoretical curves match this column density at temperatures nearly an order of magnitude lower than those inferred from CIE models, favouring a scenario in which the AAL gas traced by O IV is predominantly photoionized.

$\log(n_{\rm H}/{\rm cm}^{-3}) = 2.8$, and solar metallicity, for a range of ionization parameters U, holding T constant, and repeating to create a grid of values (U, T). We then plot the predicted O IV column density as a function of T for a range of values of U in Fig. 12. CIE is achieved in the limit of high T and/or low U. The horizontal grey bar represents the 1σ constraint on the O IV column density in velocity component v_2. The dashed blue vertical line and accompanying arrow represents the lower limit on the temperature based on the column density ratio O IV/O V. This is then an indication of the characteristic temperature of the gas hosting O IV in CIE. Temperatures to the right of the red dashed line at $10^{5.5}$ K have already been ruled out based on the observed line widths (see Fig. 7).

Given the lower and upper bounds on the gas temperature, it is clear that the predicted O IV column density in Fig. 11 is at least an order of magnitude larger than that observed. All theoretical

curves match the observed O IV column density for $T \lesssim 10^{4.85}$ K. We note that decreasing U further has no effect on this result, since by $\log U = -5$, the solution has converged to a value $T \approx 10^{4.85}$ K. The assumed H I column density is close to the maximum allowed by the data, although this value would have to be reduced by at least an order of magnitude to give agreement between the predicted temperatures. Similarly, the metallicity would have to be lowered by at least an order of magnitude. In photoionization equilibrium, the ionization parameter for the gas traced by O IV is $\log U \sim -2$, which upon inspection of Fig. 12 gives a temperature of $T \approx 10^{4.5}$ K, fully consistent with that predicted by the photoionization models. Changing the incident continuum to the 'Soft X-ray peak' model gives similar results. We therefore conclude that the AAL gas traced by O IV (and ions with similar ionization potential) is predominantly photoionized. We are not able to rule out CIE in the more highly ionized species like Ne VIII and Mg X, since the required temperatures would produce negligible accompanying O IV absorption, below the detection limits of the present data.

4.4 Gas metallicity and total column density

The metallicity $[M/\mathrm{H}]$ of the gas giving rise to the AALs can be expressed as

$$\left[\frac{M}{\mathrm{H}}\right] = \log\left(\frac{N(M_i)}{N(\mathrm{H\,I})}\right) + \log\left(\frac{f(\mathrm{H\,I})}{f(M_i)}\right) + \log\left(\frac{\mathrm{H}}{M}\right)_{\odot} \quad (19)$$

(Hamann & Ferland 1999), where $(\mathrm{H}/M)_{\odot}$ is the solar abundance ratio of hydrogen to some metal species M, $N(\mathrm{H\,I})$ and $f(\mathrm{H\,I})$, respectively, are the column density and ionization fraction in H I, and $N(M_i)$ and $f(M_i)$, respectively, are the column density and ionization fraction in some ion M_i of metal species M. If the gas is well characterized by a single ionization parameter, equation (19) can be implemented using the measured column densities in hydrogen and some arbitrary metal ion, together with the inferred ionization fractions in each, and assuming solar abundance ratios. When there is a range in ionization parameter, the situation is more complicated, since the measured column density in each ion will be the sum of the column densities arising in each region (each characterized by a different value of U). In this case, the measured column density in some ion M_i will be expressed as

$$N(M_i) = \sum_k N(M)_k f(M_i)_k, \quad (20)$$

where $N(M)_k$ and $f(M_i)_k$ are the k total column densities of element M, and ionization fractions of ion M_i, respectively, for a set of k ionization parameters. In the limit where there is a continuous distribution over ionization parameter, this becomes

$$N(M_i)_{\mathrm{obs}} = \int_{\xi_{\mathrm{min}}}^{\xi_{\mathrm{max}}} \frac{\mathrm{d}N(M)}{\mathrm{d}\xi} f(M_i)\,\mathrm{d}\xi, \quad (21)$$

where $\xi = \log U$.

To estimate total column densities in velocity components v_2 and v_4 (where we have the largest number of well-measured ions), we assume that all of the gas is photoionized, and plot the locus of points that mark the observed column densities in $\log U$–$\log N_{\mathrm{H}}$ space as shown in Figs 13 and 14, where the width of each contour indicates the 1σ uncertainty. The left-hand panels represent the case where the gas is photoionized by the 'UV peak' SED, with assumed metallicities $[M/\mathrm{H}] = -2, -1, 0$ and 1. The right-hand panels represent the equivalent scenario, but with the 'Soft X-ray peak' SED. Various zones within the absorbing region are physically characterized by the pair (U, N_{H}) that best predict the observed column densities. Constraints on the ionization parameter are identified on the basis of column density ratios that are labelled similarly to those in Fig. 10. Ratios that involve one ion having a lower limit on the column density give corresponding lower limits on the ionization parameter in Figs 13 and 14, plotted with the vertical dashed lines and corresponding arrows. In velocity component v_2, we identify a minimum of two ionization components (U, N_{H}) that can account for all of the observed column densities. Ionization parameters in these components are inferred from the ratios $N(\mathrm{O\,IV})/N(\mathrm{Ar\,VIII})$ and $N(\mathrm{Ne\,VIII})/N(\mathrm{Mg\,X})$. This conclusion comes with the caveat that we require there to be an underabundance of nitrogen (and an overabundance of sulphur, in the case of the UV peak SED) by factors of a few with respect to the solar values to explain why the O IV, N IV, S V and Ar VIII contours do not all cross in the $\log U$ range defined by $N(\mathrm{O\,IV})/N(\mathrm{Ar\,VIII})$. In velocity component v_4, we require there to be at least three ionization components, with a similar caveat on the assumed overabundance of sulphur. This result contrasts with that from some previous, similar studies, that find that a maximum of two discrete ionization components are required to adequately fit the data (e.g. Moe et al. 2009; Edmonds et al. 2011; Borguet et al. 2012; Arav et al. 2013). In this case, the ionization components inferred are no longer robust, since there are non-negligible fractional abundances of e.g. O IV and N IV in both of the lower ionization components. The limiting scenario, is one where there exists a continuous distribution of ionization parameters through the absorbing region, which at a fixed distance R corresponds to a smooth variation in gas density. This scenario is described by equation (21). To simplify the problem, we assume that a (close-to) continuous distribution in U exists in the AAL region, and find an approximate solution to equation (21) assuming that each ion forms largely at the peak in its fractional abundance, $f(M_i)_{\mathrm{max}}$. In this case, equation (21) becomes

$$N(M) \simeq \frac{N(M_i)}{f(M_i)_{\mathrm{max}}}, \quad (22)$$

and we can read off a corresponding ionization parameter from Fig. 10.

Assuming that most of the gas hosting H I also hosts most of the low-ionization species in our sample (e.g. N III, N IV, O IV and S V), we can identify peak fractional abundances of these ions with fractional abundances of H I in Fig. 10 and find the metallicity of the gas using equation (19). Incorporating uncertainty in the SED, we conservatively conclude that $0 \lesssim [\mathrm{O/H}] \lesssim 1$. We find this metallicity to be representative across all velocity components, and find the same result for [N/H] and [S/H]. Peak fractional abundances correspond to column density loci minima in Figs 13 and 14. Splitting the $\log U$ range in half at $\log U = -1$, it is clear that the high-ionization gas traced by e.g. Ne VIII and Mg X has a factor of $\sim$10 higher contribution to the total column density compared to the low-ionization gas traced by e.g. N III and O IV. Constructing plots like these for all other velocity components (not shown), we conservatively conclude that, for each of the velocity components v_1–v_7, the total hydrogen column density is $10^{17} \lesssim N_{\mathrm{H}} \lesssim 10^{18.5}$ cm^{-2} in the low-ionization gas, and $10^{18.5} \lesssim N_{\mathrm{H}} \lesssim 10^{20}$ cm^{-2} in the high-ionization gas. In velocity component v_8 we detect only O IV, O V and N IV absorption, and the total hydrogen column density through this region is, conservatively, $10^{16.5} \lesssim N_{\mathrm{H}} \lesssim 10^{17.5}$ cm^{-2}.

4.5 Distance and size constraints

Given the estimate on n_{H}, combined with information on U and N_{H}, we can put a constraint on both the distance to the absorbing clouds

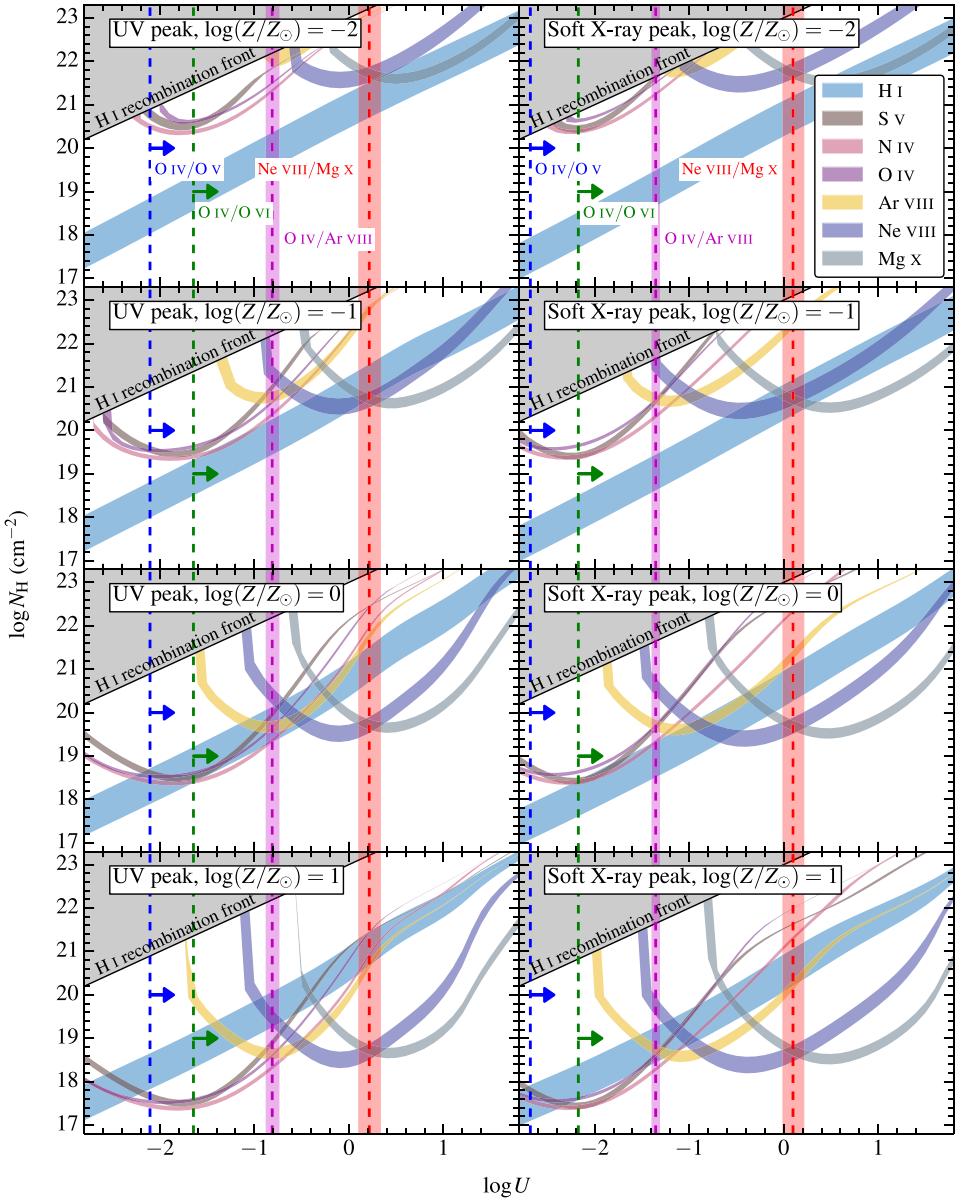

Figure 13. Ionization solutions for component v_2 in the case of the 'UV peak' incident SED (left-hand panels) and the 'Soft X-ray peak' SED (right-hand panels) for a range of metallicities. Coloured regions represent the values of $\log U$ and $\log N_{\rm H}$ that predict the $\pm 1\sigma$ bounds on the column densities for each labelled ion. The vertical bars indicate the plausible range in U for each of the ionization components identified by the column density ratios labelled. The crossing points between contours, defining the pair (U, $N_{\rm H}$) physically characterize these components. The dashed vertical lines and arrows represent lower limits on U.

from the QSO and their geometry. To determine the distance, R, we simply rearrange equation (18) to obtain

$$R = \sqrt{\frac{Q_{\rm H}}{4\pi c n_{\rm H} U}}, \tag{23}$$

where

$$Q_{\rm H} \equiv \int_{\nu_{\rm LL}}^{\infty} \frac{L_\nu}{h\nu} {\rm d}\nu \tag{24}$$

expresses the rate of emission of photons having energies sufficient to ionize hydrogen. Incorporating the uncertainty in $Q_{\rm H}$ (due to uncertainties in the SED), and conservatively estimating from Fig. 10 that absorption due to O IV and O IV* is expected to arise in gas with $-2.4 \lesssim \log U \lesssim -2.0$ (from peak fractional abundances), we find that $2.3 \lesssim R \lesssim 6.0$ kpc. Since the velocity structure is consistent with being the same across all ions, this distance is likely to be representative for the AAL region as a whole. Therefore, if all of the gas were photoionized, given the expression for U in equation (18), we should expect clouds with differing densities. The ionization parameter is around two orders of magnitude different between the gas hosting the majority of O IV and the gas hosting the most highly ionized species (Ne VIII, Mg X), so this gas should have a characteristic density around two orders of magnitude smaller, i.e. $n_{\rm H} \sim 10\,{\rm cm}^{-3}$. We note that the most highly ionized species may also form at temperatures higher than those typical of photoionization equilibrium. In such a case, densities may be higher than implied by the reasoning presented above.

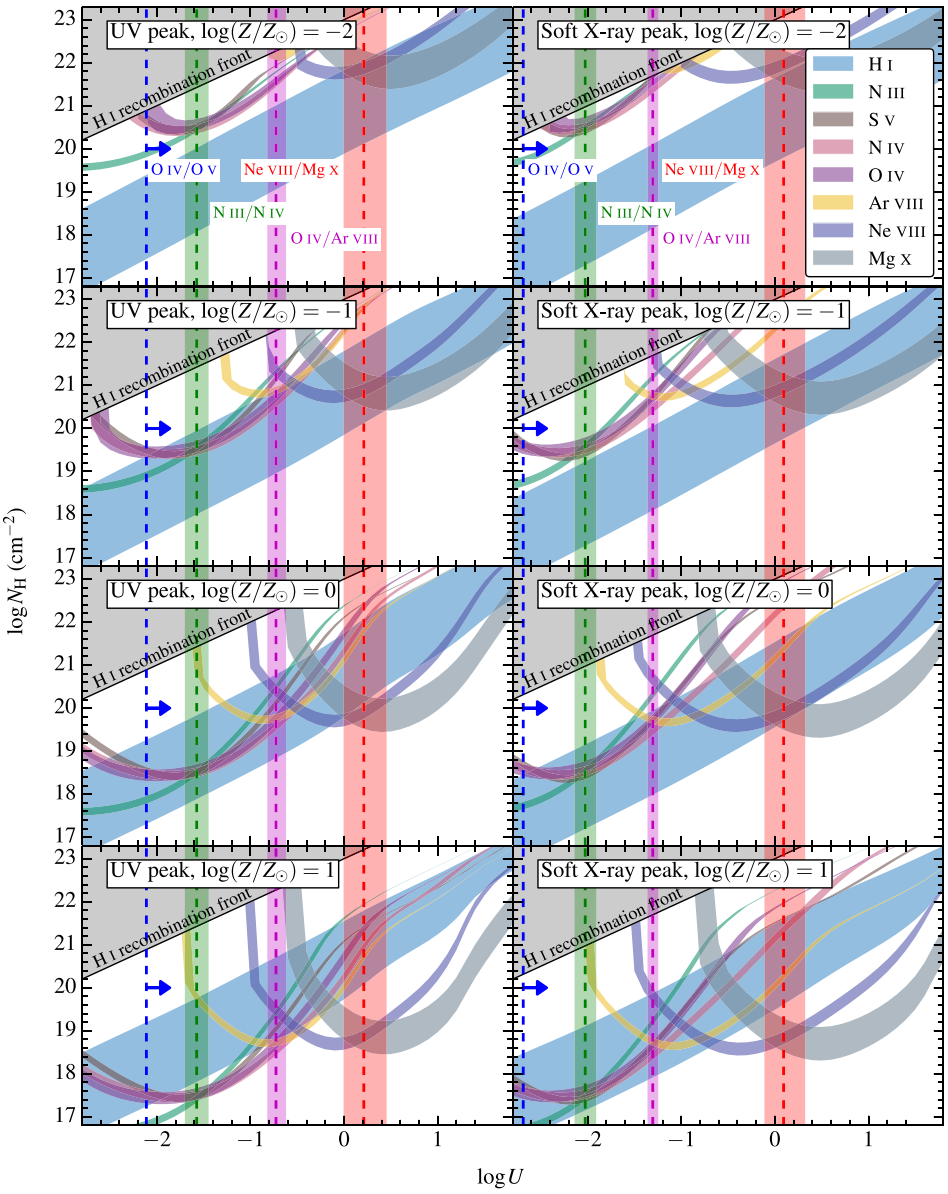

Figure 14. Ionization solutions for component v_4 in the case of the 'UV peak' incident SED (left-hand panels) and the 'Soft X-ray peak' SED (right-hand panels) for a range of metallicities. This figure has the same format as Fig. 13.

We can now estimate the absorption path length through the AAL region as $l_{\rm abs} = N_{\rm H}/n_{\rm H}$. Adopting $n_{\rm H} \sim 10^3\,{\rm cm}^{-3}$ through the least ionized gas ($10^{17} \lesssim N_{\rm H} \lesssim 10^{18.5}\,{\rm cm}^{-2}$) and $n_{\rm H} \sim 10\,{\rm cm}^{-3}$ through the most highly ionized gas we detect ($10^{18.5} \lesssim N_{\rm H} \lesssim 10^{20}\,{\rm cm}^{-2}$), we derive characteristic absorption path lengths of $10^{-4.5} \lesssim l_{\rm abs} \lesssim 10^{-3}$ and $0.1 \lesssim l_{\rm abs} \lesssim 1$ pc, respectively, in each velocity component. Note that the absorption path length is even smaller for velocity component v_8. If we assume that the absorbing gas completely fills the volume it encompasses, then these path lengths are also representative of the cloud sizes along the line of sight. If instead there are many clouds contributing to the total column density in each component, then the cloud sizes will be *smaller*, and the volume they encompass *larger* than the absorption path length. Additionally, based on indications in Section 3.1 that the QSO continuum is only partially covered by the absorbing clouds, the transverse sizes of these gas clouds are likely to be $l_{\rm trans} \lesssim 10^{-2.5}$ pc (Jimenez-Vicente et al. 2012).

5 DISCUSSION AND CONCLUSIONS

The main results from the data analysis and photoionization/CIE models are as follows.

(i) The gas in the least ionized AAL region is predominantly photoionized.

(ii) Under photoionization equilibrium, multiple ionization parameters are required to reproduce the column density ratios seen in the data.

(iii) Based on the observed column densities and ionization fractions implied from characteristic ionization parameters, incorporating uncertainties in the shape of the QSO SED, the gas metallicity is conservatively $0 \lesssim {\rm [O/H]} \lesssim 1$.

(iv) Given the range in possible gas metallicity, the total hydrogen column density in each velocity component is $10^{17} \lesssim N_{\rm H} \lesssim 10^{18.5}\,{\rm cm}^{-2}$ in the least ionized gas (with slightly smaller values for

velocity component v_8) and $10^{18.5} \lesssim N_{\rm H} \lesssim 10^{20}\,{\rm cm}^{-2}$ through the most highly ionized gas we detect.

(v) Taking the column density ratio between O IV* and O IV, assuming the fine-structure excited states are populated mostly due to collisions with electrons, the total hydrogen density in the gas traced by these ions is found to be $\log(n_{\rm H}/{\rm cm}^{-3}) \sim 3$ for solar metallicity.

(vi) Given the total hydrogen density, and the plausible range in ionization parameter for the gas traced by O IV and O IV*, the distance to the absorbing clouds from the centre of the QSO is found to be $2.3 \lesssim R \lesssim 6.0\,{\rm kpc}$. An empirically identified, shared velocity structure amongst all ions, suggests that this distance determination is likely to be representative for the AAL region as a whole.

(vii) Under photoionization equilibrium, the total hydrogen density in the most highly ionized AAL gas is found to be two orders of magnitude lower than that implied for the low-ionization gas. Alternatively, models in which this gas is under CIE allow for densities to be similar across the AAL region probed by these data.

(viii) The ratio $N_{\rm H}/n_{\rm H}$ sets limits on the absorption path length through the least and mostly highly ionized regions we detect of $10^{-4.5} \lesssim l_{\rm abs} \lesssim 10^{-3}$ and $0.1 \lesssim l_{\rm abs} \lesssim 1\,{\rm pc}$, respectively, in each velocity component.

(ix) Covering fractions less than unity (in all cases where they can be reliably measured), suggest that the continuum region is only partially covered, requiring clouds with transverse sizes $l_{\rm trans} \lesssim 10^{-2.5}\,{\rm pc}$.

In summary, the analysis of the previous sections has revealed the presence of metal enriched (to at least solar), highly ionized gas clouds a few kpc from the centre of Q0209 that are likely to be very small (sub-pc scale). In the following sections we place these results in a wider context, and speculate on the origins and fate of the absorbing gas. For simplicity, we shall speak of two, co-spatial regions in ionization equilibrium: a low-ionization, photoionized region with $\log U \lesssim -1$ and a high-ionization region with $\log U \gtrsim -1$ if photoionized, or temperatures $T \gtrsim 10^{5.5}\,{\rm K}$ if collisionally ionized.

5.1 Gas structure and dynamics

A redshift measurement for Q0209 of $z_{\rm QSO} = 1.131\,94 \pm 0.000\,01$ implies that the AAL gas is mostly outflowing from the QSO with velocities up to $\sim$400 km s^{-1} (see Fig. 8). This is unusually small, compared to the majority of the AALs and BALs in the literature with high-ionization species such as Ne VIII and Mg X, which are typically outflowing with velocities closer to a few thousand or few tens of thousand km s^{-1} (e.g. Hamann et al. 1995; Telfer et al. 1998; Arav et al. 1999; Petitjean & Srianand 1999; Muzahid et al. 2012, 2013), although see Hamann et al. (2000) for a more similar example. If we assume that the gas is moving with a constant radial velocity v and originates close to the SMBH, then the time-scale for reaching its current radius R is at least

$$t \approx 10^7 \left(\frac{R}{2.3\,{\rm kpc}}\right)\left(\frac{200\,{\rm km\,s^{-1}}}{v}\right)\,{\rm yr}. \quad (25)$$

Different velocity components in the AAL gas are moving at different speeds, so the overall region should possess an appreciable radial thickness after a time t, even though we derive densities and ionization parameters that are consistent with one another across the different velocity components.

Given the small cloud sizes in the low-ionization gas, a key question is how long they are expected to survive. The free-fall time-scale for these clouds can approximately be expressed as

$$t_{\rm ff} \equiv \frac{1}{\sqrt{G\rho}} \sim 1.0 \times 10^{15}\,{\rm s}\left(\frac{n_{\rm H}}{{\rm cm}^{-3}}\right)^{-1/2}, \quad (26)$$

where G is the gravitational constant, ρ is the gas density, assuming that all of the mass is baryonic, and setting the mass fraction in helium to 0.28 (assuming solar abundances). In addition, for a characteristic cloud size l, the sound crossing time in a highly ionized plasma can be approximated by

$$t_{\rm sc} \equiv \frac{l}{c_{\rm s}} \sim 2.1 \times 10^{15}\,{\rm s}\left(\frac{l}{\rm kpc}\right) T_4^{-1/2}, \quad (27)$$

where $c_{\rm s}$ is the sound speed in an ideal monatomic gas and $T = T_4 \times 10^4\,{\rm K}$ (e.g. Schaye 2001). For a stable cloud in hydrostatic equilibrium, $t_{\rm sc} \sim t_{\rm ff}$. We take a value of $n_{\rm H} = 10^3\,{\rm cm}^{-2}$ and a value of $l = 10^{-6}\,{\rm kpc}$ (assuming $l_{\rm abs} \approx l$). The photoionization models indicate that $T_4 \approx 2$ in this gas and so we find $t_{\rm ff} \sim 3.2 \times 10^{13}\,{\rm s} \gg t_{\rm sc} \sim 1.5 \times 10^9\,{\rm s}$. This implies that the clouds will expand on the sound crossing time-scale, so they should have lifetimes of $\lesssim$100 yr. This is considerably less than the characteristic flow time in equation (25), and so the probability of observing these clouds at their implied distance from the QSO is extremely small in this case.

The analysis presented above poses a problem, which may be overcome if the clouds are being held in pressure equilibrium. This may be a thermal pressure equilibrium with higher temperature, lower density, more highly ionized gas, equivalent to the statement $n_{\rm H1}T_1 = n_{\rm H2}T_2$, where $n_{\rm H1}$, T_1 and $n_{\rm H2}$, T_2 are the total hydrogen densities and temperatures of the low- and high-ionization regions, respectively. From Section 4, under photoionization equilibrium we found that $n_{\rm H2} \sim 10\,{\rm cm}^{-2}$, and these models also indicate that $T_2 \approx 6 \times 10^4\,{\rm K}$. In this case, $n_{\rm H1}T_1 > n_{\rm H2}T_2$, and the high-ionization gas cannot pressure support the low-ionization gas. If the former is collisionally ionized, we now have temperatures that differ by more than an order of magnitude. Densities in the high-ionization region may be low enough to allow for pressure support. Nevertheless, the high-ionization gas itself, accounting for the possibility that it is photoionized, should have a lifetime $\lesssim 10^5$ yr, which is still short enough to suggest that this gas may also require pressure support from even more highly ionized gas that we do not detect in the UV, and which would require larger total column density, higher temperature and lower density.

Massive galaxies are expected to host hot gas coronae, well within the implied location of the AAL region, with $T \sim 10^6\,{\rm K}$ and $n_{\rm H} \sim 10^{-2}\,{\rm cm}^{-2}$ (e.g. White & Frenk 1991; Fukugita & Peebles 2006). Pressure from this external medium, together with additional pressure support from magnetic confinement (de Kool & Begelman 1995) may help to alleviate the problems outlined above, although pressure supporting gas with varying internal pressure is clearly a complex issue. We note that the analysis above does not incorporate the effects of turbulence, which is almost certainly present given the observed line widths (see Section 3.2). In addition, gas outflowing from a QSO will likely encounter the interstellar medium (ISM) of the host galaxy on its journey out into the halo. At supersonic velocities, shocks will likely occur at the interface between the outflowing gas and the ISM, heating the gas close to this interface. The resulting mix of hot and cool gas creates instabilities that can destroy the clouds before they reach the halo (see e.g. arguments in Faucher-Giguère, Quataert & Murray 2012). These authors suggest an alternative scenario, in which small clouds may be formed in situ from moderately dense ISM clouds within hot, recently shocked gas.

These clouds become shredded by a passing blast wave and gain momentum from an accompanying shock. The resulting 'cloudlets' in this model have sizes and densities comparable to those derived here, and can possess a range of velocities that may explain the multicomponent velocity structure in the absorption profiles.

Models such as these may offer a more promising route to explain the structure and dynamics of AALs with properties (density, cloud size, velocity structure, distance from the QSO) similar to those found in Q0209 (e.g. Petitjean & Srianand 1999; Hamann et al. 2000; Edmonds et al. 2011; Borguet et al. 2012; Arav et al. 2013; Muzahid et al. 2013). Any viable model must additionally reproduce the covering fractions seen in the present data. Covering fractions less than unity, and with little variation, are seen in ions spanning a range in ionization potential from a few tens to a few hundreds of eV, tracing gas with more than one possible ionization mechanism. Vastly differing absorption path lengths through the AAL region, as hinted at in the analysis of the previous sections, make it very difficult to account for the near constancy in covering fraction across all ions using simple geometrical models. We also note that these results differ from e.g. Hamann et al. (2000) and Borguet et al. (2012), who find more complete coverage in high-ionization UV transitions compared to those at lower ionization potentials. Covering fractions less than unity across our sample also go against general trends for more complete coverage with lower outflow velocities, as identified in the COS sample presented by Muzahid et al. (2013). It is therefore clear that simple trends such as these may not produce robust predictions for individual systems, which further highlights the apparent complexity in these absorbers.

5.2 Are the AAL clouds out of equilibrium?

Up to this point, our analysis and discussion has assumed that the AAL clouds are in ionization equilibrium. However, in general, absorbers may be out of equilibrium when close to an AGN, due to recombination time-scales that can be long compared to typical AGN lifetimes and duty cycles (e.g. Krolik & Kriss 1995; Nicastro et al. 1999; Arav et al. 2012; Oppenheimer & Schaye 2013a,b). The resulting recombination lag can lead to situations where high-ionization stages like O VI, Ne VIII and Mg X are enhanced relative to the expectation from equilibrium models. We examine these issues here.

We define the photoionization rate Γ_{M_i} (s^{-1}) for a given ion M_i as

$$\Gamma_{M_i} \equiv \int_{\nu_{0,M_i}}^{\infty} \frac{4\pi J_\nu}{h\nu} \sigma_{M_i}(\nu)\, \mathrm{d}\nu. \quad (28)$$

Here ν is the frequency, ν_{0,M_i} is the ionization frequency, J_ν is the intensity of the QSO radiation field (erg s^{-1} cm^{-2} Hz^{-1} sr^{-1}), σ_{M_i} is the photoionization cross-section and h is Planck's constant. The recombination rate (s^{-1}) into an ion M_i is given by

$$R_{M_i} \equiv \alpha_{M_i} n_\mathrm{e}, \quad (29)$$

where n_e is the electron number density and α_{M_i} is the temperature dependent recombination rate coefficient (cm^3 s^{-1}) for that ion. Finally, the collisional ionization rate for an ion M_i is

$$C_{M_i} \equiv \beta_{M_i} n_\mathrm{e}, \quad (30)$$

where β_{M_i} is the temperature dependent collisional ionization rate coefficient (cm^3 s^{-1}). Neglecting Auger ionization and charge transfer, the population in an ion M_i is then

$$\frac{\mathrm{d}n_{M_i}}{\mathrm{d}t} = -n_{M_i}(\Gamma_{M_i} + R_{M_{i-1}} + C_{M_i}) + n_{M_{i+1}} R_{M_i} + n_{M_{i-1}}(\Gamma_{M_{i-1}} + C_{M_{i-1}}). \quad (31)$$

Now suppose that an absorber is in photoionization equilibrium, i.e. $\mathrm{d}n_{M_i}/\mathrm{d}t = 0$, at time $t = 0$, but there is a sudden change in the ionizing flux, such that $\Gamma_{M_i}(t > 0) = (1 + \delta)\Gamma_{M_i}(t = 0)$, where $-1 \leq \delta \leq \infty$. Taking the collisional ionization rate to be negligible (a reasonable approximation for a photoionized plasma), it can then be shown that the e-folding time-scale for change in the ionic fraction is given by

$$t_\mathrm{change} = \left[-\delta \alpha_{M_i} n_\mathrm{e} \left(\frac{n_{M_{i+1}}}{n_{M_i}} - \frac{\alpha_{M_{i-1}}}{\alpha_{M_i}} \right) \right]^{-1}, \quad (32)$$

(Arav et al. 2012), where negative time-scales indicate a decrease in the ionic fraction, and positive time-scales indicate an increase. For changes in the ionizing flux within an order of magnitude ($0.1 < 1 + \delta < 10$), these time-scales are typically $\sim$10 yr for the densities implied by the O IV* analysis of Section 4.1, assuming $T \sim 10^4$ K. Since the gas densities in the AAL region are much higher than those typical of the diffuse IGM and circumgalactic medium, these time-scales are much shorter than the typical AGN lifetime ($\sim$ Myr time-scales; e.g. Novak, Ostriker & Ciotti 2011). Therefore, photoionization equilibrium might be a valid assumption in our case, so long as these time-scales are also short compared to the time-scale over which the QSO luminosity changes.

However, we must also consider the dynamical evolution of the AAL clouds. In the previous section, we found that, unless the clouds traced by O IV are pressure supported by an external medium, they will expand on time-scales $\lesssim$100 yr. If this process is occurring, then the clouds may be entering a non-equilibrium state due to a recombination lag. To determine whether or not this scenario is likely, we numerically solve the coupled, time-dependent ionization equations (equation 31) for a set of elements using a fourth-order Runge–Kutta method. We assume that the AAL region possesses a gas density of $n_\mathrm{H} = 10^3$ cm^{-3} and is illuminated by the 'UV peak' SED at a distance of 2.3 kpc. Assuming a gas temperature $T = 10^4$ K, we then calculate recombination rate coefficients using the Badnell (2006) fits (assuming case A recombination), and collisional ionization rate coefficients using the data in Voronov (1997). We perform the integral in equation (28) using the same photoionization cross-sections as used in CLOUDY c13.00. Equilibrium values of n_{M_i} are then calculated, assuming solar abundances. We assume these values to hold at a time $t = 0$. We next perturb the gas density such that $n(t > 0) = (1 + \delta)n(t = 0)$, where $-1 \leq \delta \leq \infty$, identical to the case of flux changes considered above. We do this for four different values of $(1 + \delta) = 0.1$, 0.01, 0.001 and 10. The latter is included for the interest of comparing both increasing and decreasing density. For example, if the AAL clouds are the result of shocked ISM clouds, we might expect them to be crushed prior to their subsequent expansion (e.g. Faucher-Giguère et al. 2012). The resulting time-dependent evolution in the number density of H I, O IV, O V, O VI, Ne VIII and Mg X is shown in Fig. A2 in Appendix A.

Simple inspection of Fig. A2 indicates that, for a decrease of more than an order of magnitude in gas density, with the exception of H I, time-scales for reaching a new equilibrium are >100 yr. Comparing this to the expansion time-scale, we conclude that non-equilibrium effects are important if the density in the AAL region is dropping by orders of magnitude. Time-scales are orders of magnitude shorter for an increase in density, and so we expect that a decrease in density should form the dominant contribution

to any non-equilibrium behaviour. We note that the situation described is not physical – we expect a smooth change in density with time, not a step function change. Nevertheless, lacking a physical motivation for the exact functional form, we present these results as an approximation. The non-equilibrium behaviour shown in Fig. A2 indicates considerable variation in the rate of change of ionic number density, with the more highly ionized species changing more rapidly. Under photoionization equilibrium, the AAL region was found to possess a range in density and absorption path length covering orders of magnitude. This situation was required due to the co-spatial existence of ionic species tracing gas with multiple ionization parameters. If ionic number densities are changing at highly variable rates, then it is possible to envisage scenarios whereby the fractional abundances of ions spanning a large range in ionization potential can all be high. We therefore speculate that it may be possible to find non-equilibrium models that reproduce all of the observed column densities in a single phase, with a single density and absorption path length. Such a scenario may be desirable, as it is in better concordance with the near constant covering fraction seen across these ions.

It is important to note that the calculations leading to inferred cloud lifetimes of $\lesssim$100 yr assume that the cloud sizes l are approximately equal to the absorption path length $l_{\rm abs}$. However, in general, $l < l_{\rm abs}$, which would make the cloud lifetimes even shorter. Scenarios where $l < l_{\rm abs}$ have been put forward multiple times in the literature, typically to explain situations where the derived covering fractions in the data depend on velocity across the absorption profiles, and the ionization and/or true optical depth in the lines. This situation is referred to as inhomogenous partial coverage (e.g. de Kool, Korista & Arav 2002; Hamann & Sabra 2004; Arav et al. 2008), where there are many small clouds having a power-law dependence in optical depth across their transverse extent. Covering fractions that vary in the way just described are not found in our data. Nevertheless, we cannot rule out the possibility that there are multiple small clouds along the line of sight. In such a scenario, the case for non-equilibrium evolution in the ionic number densities becomes more compelling.

In summary, if the AAL region is not pressure supported, then simple analytical arguments suggest that non-equilibrium effects may be important in these clouds. A cloud expansion time-scale of $\lesssim$100 yr is sufficiently short, that these effects might be confirmed with repeat observations. These observations will be crucial in determining appropriate non-equilibrium models for the data.

5.3 The connection to associated X-ray absorption

We next consider the link between associated UV absorption and so-called 'warm absorbers', often characterized by both bound–bound and bound–free absorption in X-rays. A key question is whether or not this absorption is predicted by the UV absorption lines characterized here. In the most highly ionized gas, under photoionization equilibrium, the maximum predicted total hydrogen column density is $\log(N_{\rm H}/{\rm cm}^{-2}) \approx 20$, and the ionization parameter $\log U \approx 0.5$. We assume an upper limit on the gas metallicity of [O/H] ≈ 1. Explicit photoionization calculations using these parameters predict the presence of bound–bound transitions, but no significant bound–free absorption in X-rays. The same result is obtained in CIE calculations. In this respect, and also in terms of their relatively small velocity shift from the QSO, the AALs in Q0209 are similar to those reported in e.g. Hamann et al. (2000). If there is continuous X-ray absorption, it should be in much more highly ionized gas with larger total column density. This gas may trace the bulk of an outflow that produces the gas condensations described in the previous section. However, in general, the gas giving rise to warm absorbers need not be co-spatial with UV and/or optical AALs, especially since these absorption systems arise in gas with a wide range of physical parameters (outflow velocities, ionization, covering fractions, distance from the QSO etc.; see e.g. Ganguly et al. 1999; Misawa et al. 2007; Nestor et al. 2008; Ganguly et al. 2013; Muzahid et al. 2013; Sharma, Nath & Chand 2013). It is intriguing nonetheless, that the AALs in Q0209 show nearly identical velocity component structure over ~300 eV in ionization potential, suggesting that absorption lines from many ionization stages can indeed arise co-spatially. Simultaneous observations in the UV and X-rays will likely be required to gain deeper insights into the connection between warm absorbers and AALs in general (e.g. Di Gesu et al. 2013; Lee et al. 2013).

5.4 Outflow models

Before considering potential origins for the outflowing gas, we first perform a rough estimate of the mass and kinetic energy in the AALs. We assume the geometry of the outflowing gas traced by these data to be that of a thin, partially filled shell of material moving radially outwards from the centre of the QSO, the flux from which is modelled by the 'UV peak' SED. Under this geometry, the mass depends on the distance from the QSO ($R \sim 2.3$ kpc), the total column density through the AAL region (we find a value $N_{\rm H} \approx 2 \times 10^{20}\,{\rm cm}^{-2}$), and crucially, the global covering fraction, Ω, of the AAL gas, as opposed to the line of sight covering fraction that we measure. A rough estimate of this quantity comes from the incidence rate of associated absorption systems like that seen in Q0209. Muzahid et al. (2013) presented a sample of 20 QSO spectra observed with COS, from which associated absorbers were selected based on the presence of Ne VIII absorption. The incidence rate of these absorption systems was found to be 40 per cent, and we consider this to be the closest representative sample in the literature at present, although the general conclusions below are not sensitive to this value. We therefore express the total gas mass in the UV AAL region as

$$M \approx 6 \times 10^{7} \left(\frac{\Omega}{0.4}\right) \left(\frac{N_{\rm H}}{2 \times 10^{20}\,{\rm cm}^{-2}}\right) \left(\frac{R}{2.3\,{\rm kpc}}\right)^{2} {\rm M}_{\odot}, \quad (33)$$

where we have assumed a mean molecular weight per proton of $\mu_{\rm H} = 1.4$. The total kinetic energy in this gas is then

$$K \approx 2 \times 10^{55} \left(\frac{M}{6 \times 10^{7}\,{\rm M}_{\odot}}\right) \left(\frac{v}{200\,{\rm km\,s}^{-1}}\right)^{2} {\rm erg}. \quad (34)$$

We can derive the average mass outflow rate $\dot{M}$, by dividing M by the dynamical time-scale R/v, and subsequently derive the kinetic luminosity of the gas as $\dot{K} = 0.5\dot{M}v^2$. This gives values of $\dot{M} \approx 5\,{\rm M}_{\odot}\,{\rm yr}^{-1}$ and $\dot{K} \approx 7 \times 10^{40}\,{\rm ergs}^{-1}$. It is instructive to bear in mind that, while these quantities are useful, there are good reasons to believe that the gas clouds traced by the AALs may not travel a distance R, and are instead accelerated close to their observed location (see Section 5.1).

We consider two primary sources for the gas flow generating the AALs: (i) line-driven winds, and (ii) supernova-driven winds. Line-driven winds, initially accelerated through radiation pressure from the SMBH accretion disc, are commonly invoked to explain the winds traced by BALs and AALs with velocities of a few 1000 km s^{-1}, and are a major source of energy injection into the ISM in models of AGN feedback (e.g. Scannapieco & Oh 2004;

Di Matteo et al. 2005; Hopkins & Elvis 2010). Specifically, these models require kinetic luminosities to be $\dot{K} \gtrsim 0.1$ per cent of the Eddington luminosity, $L_{\rm Edd}$. For Q0209, $\log(L/L_{\rm Edd}) \gtrsim 0$ (Done et al., in preparation), which implies the kinetic luminosity in the AALs is at least two orders of magnitude below this level. In addition, models involving line-driven winds suggest they must be launched close to the SMBH at velocities of a few $100\,{\rm km\,s^{-1}}$ (e.g. Risaliti & Elvis 2010), which is already the velocity of the AALs seen here at much larger distances. If the AALs are pressure confined in a line-driven wind such as this, they must encounter significant drag from a surrounding medium to slow them down, or keep them from accelerating to much larger velocities. In the more likely case that the AALs are formed in situ, a variety of velocities could in principle be observed. For example, in the radiative shock model of Faucher-Giguère et al. (2012), AAL clouds will take a finite time to accelerate up to the velocity of the passing blast wave (see their equation 12). Although the UV AAL clouds in Q0209 contribute only a small percentage of the kinetic luminosity required for significant AGN feedback into the surrounding ISM (and IGM), a much larger percentage may be carried by an associated, much more highly ionized warm absorber, with higher total column density, detectable as bound–free absorption in X-rays (e.g. Crenshaw et al. 2003; Gabel et al. 2005; Arav et al. 2007). We note that bound–free X-ray absorption is by no means ubiquitous, with some warm absorbers now being detected via absorption *lines* such as O VII. These can have $N_{\rm H}$ consistent with that seen in associated UV absorption lines (e.g. Di Gesu et al. 2013).

Supernova-driven winds are thought to drive fountains of gas a few kpc into the haloes of massive galaxies, some of which are then expected to fall back on ballistic trajectories (e.g. Bregman 1980; Fraternali & Binney 2006, 2008; Marinacci et al. 2010). We find that the distance, velocity and density of the AAL gas in Q0209 is typical of galactic winds (e.g. Veilleux et al. 2005; Creasey, Theuns & Bower 2013). The infalling velocity component v_8 also indicates that some of the AAL gas may be on a return trajectory back towards the disc of the QSO host. The time-scale derived in equation (25) is consistent with expected QSO lifetimes (e.g. Novak et al. 2011), so if the clouds are a result of supernova-driven winds, it is possible that these winds were launched during a starburst phase. If we assume that the starburst proceeded at $\sim 10\,{\rm M_\odot\ yr^{-1}}$ and that this star formation results in one supernova per $100\,{\rm M_\odot}$ with energy $E_{\rm SN} \sim 10^{51}$ erg, then $\dot{E} \sim 10^{42}\,{\rm ergs^{-1}}$. Only a fraction of this energy will be converted into the kinetic energy powering an outflow, and so the kinetic luminosity we derive for the AALs in Q0209 may be consistent with this simple estimation.

At present, the data are consistent with both an outflow driven by AGN and starburst activity in Q0209. Future X-ray observations of this QSO may help to distinguish between these two possibilities. In particular, associated bound–free X-ray absorption tracing gas with high total column density and kinetic luminosity would favour an origin closely tied with the AGN.

ACKNOWLEDGEMENTS

We thank Joop Schaye, Gabriel Altay and Ewan Hemingway for helpful discussions and comments, and the anonymous referee, whose suggestions improved this paper.

CWF would like to acknowledge the support of an STFC studentship (ST/J201013/1). FH acknowledges support from the USA National Science Foundation grant AST-1009628. Support for MF was provided by NASA through Hubble Fellowship grant HF-51305.01-A.

We thank the contributors to SciPy,[9] Matplotlib[10] and the Python programming language,[11] the free and open-source community, and the NASA Astrophysics Data system[12] for software and services. This work also made use of Astropy; a community-developed core Python package for Astronomy (Astropy Collaboration 2013).

The work in this paper was mainly based on observations made with the NASA/ESA *Hubble Space Telescope* under programme GO 12264, obtained at the Space Telescope Science Institute, which is operated by the Association of Universities for Research in Astronomy Inc., under NASA contract NAS 5-26555; and with the 6.5 m Magellan Telescopes located at Las Campanas Observatory, Chile.

This work also made use of the DiRAC Data Centric system at Durham University, operated by the Institute for Computational Cosmology on behalf of the STFC DiRAC HPC Facility.[13] This equipment was funded by BIS National E-infrastructure capital grant ST/K00042X/1, STFC capital grant ST/H008519/1 and STFC DiRAC Operations grant ST/K003267/1 and Durham University. DiRAC is part of the National E-Infrastructure.

The raw data from *HST*/COS may be accessed from the MAST archive.[14] Data from Magellan/FIRE are available from the lead author upon request.

REFERENCES

Aguirre A., Schaye J., Theuns T., 2002, ApJ, 576, 1
Ahn C. P. et al., 2013, ApJS, 211, 17
Altay G., Theuns T., 2013, MNRAS, 434, 748
Arav N., Korista K. T., de Kool M., Junkkarinen V. T., Begelman M. C., 1999, ApJ, 516, 27
Arav N. et al., 2007, ApJ, 658, 829
Arav N., Moe M., Costantini E., Korista K. T., Benn C., Ellison S., 2008, ApJ, 681, 954
Arav N. et al., 2012, A&A, 544, 33
Arav N., Borguet B., Chamberlain C., Edmonds D., Danforth C. W., 2013, MNRAS, 436, 3286
Astropy Collaboration et al., 2013, A&A, 558, 33
Badnell N. R., 2006, ApJS, 167, 334
Bahcall J. N., Wolf R. A., 1968, ApJ, 152, 701
Balashev S. A., Petitjean P., Ivanchik A. V., Ledoux C., Srianand R., Noterdaeme P., Varshalovich D. A., 2011, MNRAS, 418, 357
Barlow T. A., Sargent W. L. W., 1997, AJ, 113, 136
Benson A. J., Bower R. G., Frenk C. S., Lacey C. G., Baugh C. M., Cole S., 2003, ApJ, 599, 38
Borguet B. C. J., Edmonds D., Arav N., Dunn J., Kriss G. A., 2012, ApJ, 751, 107
Bower R. G., Benson A. J., Malbon R., Helly J. C., Frenk C. S., Baugh C. M., Cole S., Lacey C. G., 2006, MNRAS, 370, 645
Brandt W. N., Laor A., Wills B. J., 2000, ApJ, 528, 637
Bregman J. N., 1980, ApJ, 236, 577
Cardelli J. A., Clayton G. C., Mathis J. S., 1989, ApJ, 345, 245
Carswell R. F., Whelan J. A. J., Smith M. G., Boksenberg A., Tytler D., 1982, MNRAS, 198, 91
Creasey P., Theuns T., Bower R. G., 2013, MNRAS, 429, 1922
Crenshaw D. M., Kraemer S. B., George I. M., 2003, ARA&A, 41, 117
Cuillandre J.-C. J. et al., 2012, Proc. SPIE, 8448, 84480M
Cushing M. C., Vacca W. D., Rayner J. T., 2004, PASP, 116, 362

[9] http://www.scipy.org
[10] http://matplotlib.org
[11] http://www.python.org
[12] http://adswww.harvard.edu
[13] http://www.dirac.ac.uk
[14] http://archive.stsci.edu

D'Odorico V., Cristiani S., Romano D., Granato G. L., Danese L., 2004, MNRAS, 351, 976
de Kool M., Begelman M. C., 1995, ApJ, 455, 448
de Kool M., Korista K. T., Arav N., 2002, ApJ, 580, 54
Di Gesu L. et al., 2013, A&A, 556, 94
Di Matteo T., Springel V., Hernquist L., 2005, Nature, 433, 604
Dickey J. M., Lockman F. J., 1990, ARA&A, 28, 215
Done C., Davis S. W., Jin C., Blaes O., Ward M., 2012, MNRAS, 420, 1848
Draine B. T., 2011, Princeton Ser. Astrophys., Physics of the Interstellar and Intergalactic Medium. Princeton Univ. Press, Princeton
Edmonds D. et al., 2011, ApJ, 739, 7
Faucher-Giguère C.-A., Quataert E., Murray N., 2012, MNRAS, 420, 1347
Ferland G. J. et al., 2013, Rev. Mex. Astron. Astrophys., 49, 137
Foltz C. B., Weymann R. J., Peterson B. M., Sun L., Malkan M. A., Chaffee F. H. J., 1986, ApJ, 307, 504
Fraternali F., Binney J. J., 2006, MNRAS, 366, 449
Fraternali F., Binney J. J., 2008, MNRAS, 386, 935
Fraternali F., Marasco A., Marinacci F., Binney J. J., 2013, ApJ, 764, L21
Fukugita M., Peebles P. J. E., 2006, ApJ, 639, 590
Fumagalli M., O'Meara J. M., Prochaska J. X., Worseck G., 2013, ApJ, 775, 78
Gabel J. R. et al., 2005, ApJ, 623, 85
Gabel J. R., Arav N., Kim T. S., 2006, ApJ, 646, 742
Ganguly R., Eracleous M., Charlton J. C., Churchill C. W., 1999, AJ, 117, 2594
Ganguly R. et al., 2013, MNRAS, 435, 1233
Gehrels N., 1986, ApJ, 303, 336
Ghavamian P. et al., 2009, Preliminary Characterization of the Post-Launch Line Spread Function of COS, STScI ISR COS 2009-01, STScI, Baltimore
Gorenstein P., 1975, ApJ, 198, 95
Green J. C. et al., 2012, ApJ, 744, 60
Hall P. B., Anosov K., White R. L., Brandt W. N., Gregg M. D., Gibson R. R., Becker R. H., Schneider D. P., 2011, MNRAS, 411, 2653
Hamann F. W., 1997, ApJS, 109, 279
Hamann F. W., Ferland G., 1993, ApJ, 418, 11
Hamann F. W., Ferland G., 1999, ARA&A, 37, 487
Hamann F., Sabra B., 2004, in Gordon T. R., Patrick B. H., eds, ASP Conf. Ser. Vol. 311, AGN Physics with the Sloan Digital Sky Survey. Astron. Soc. Pac., San Francisco, p. 203
Hamann F. W., Barlow T. A., Beaver E. A., Burbidge E. M., Cohen R. D., Junkkarinen V., Lyons R., 1995, ApJ, 443, 606
Hamann F. W., Netzer H., Shields J. C., 2000, ApJ, 536, 101
Hamann F. W., Barlow T. A., Chaffee F. C., Foltz C. B., Weymann R. J., 2001, ApJ, 550, 142
Hamann F., Chartas G., McGraw S., Rodriguez Hidalgo P., Shields J., Capellupo D., Charlton J., Eracleous M., 2013, MNRAS, 435, 133
Hopkins P. F., Elvis M., 2010, MNRAS, 401, 7
Jimenez-Vicente J., Mediavilla E., Muñoz J. A., Kochanek C. S., 2012, ApJ, 751, 106
Jin C., Ward M., Done C., Gelbord J., 2012, MNRAS, 420, 1825
Kalberla P. M. W., Burton W. B., Hartmann D., Arnal E. M., Bajaja E., Morras R., Pöppel W. G. L., 2005, A&A, 440, 775
Kaspi S. et al., 2002, ApJ, 574, 643
Keeney B. A., Danforth C. W., Stocke J. T., France K., Green J. C., 2012, PASP, 124, 830
King A., 2003, ApJ, 596, L27
Kriss G. A., 2011, Improved Medium Resolution Line Spread Functions for COS FUV Spectra, STScI ISR COS 2011-01, STScI, Baltimore
Krolik J. H., Kriss G. A., 1995, ApJ, 447, 512
Lee J. C. et al., 2013, MNRAS, 430, 2650
Marinacci F., Binney J. J., Fraternali F., Nipoti C., Ciotti L., Londrillo P., 2010, MNRAS, 404, 1464
Mathur S., Wilkes B., Elvis M., Fiore F., 1994, ApJ, 434, 493
Mathur S., Wilkes B., Elvis M., 1998, ApJ, 503, L23
Matsuoka K. et al., 2013, ApJ, 771, 64
Mazzotta P., Mazzitelli G., Colafrancesco S., Vittorio N., 1998, A&AS, 133, 403
Misawa T., Charlton J. C., Eracleous M., Ganguly R., Tytler D., Kirkman D., Suzuki N., Lubin D., 2007, ApJS, 171, 1
Moe M., Arav N., Bautista M. A., Korista K. T., 2009, ApJ, 706, 525
Morris S. L., Weymann R. J., Foltz C. B., Turnshek D. A., Shectman S., Price C., Boroson T. A., 1986, ApJ, 310, 40
Muzahid S., Srianand R., Savage B. D., Narayanan A., Mohan V., Dewangan G. C., 2012, MNRAS, 424, L59
Muzahid S., Srianand R., Arav N., Savage B. D., Narayanan A., 2013, MNRAS, 431, 2885
Nicastro F., Fiore F., Perola G. C., Elvis M., 1999, ApJ, 512, 184
Nestor D., Hamann F., Rodriguez Hidalgo P., 2008, MNRAS, 386, 2055
Novak G. S., Ostriker J. P., Ciotti L., 2011, ApJ, 737, 26
Oppenheimer B. D., Schaye J., 2013a, MNRAS, 434, 1063
Oppenheimer B. D., Schaye J., 2013b, MNRAS, 434, 1043
Osterman S. et al., 2011, Ap&SS, 335, 257
Ostriker J. P., Choi E., Ciotti L., Novak G. S., Proga D., 2010, ApJ, 722, 642
Petitjean P., Srianand R., 1999, A&A, 345, 73
Petitjean P., Rauch M., Carswell R. F., 1994, A&A, 291, 29
Risaliti G., Elvis M., 2010, A&A, 516, 89
Sargent W. L. W., Boksenberg A., Young P., 1982, ApJ, 252, 54
Scannapieco E., Oh S. P., 2004, ApJ, 608, 62
Schaye J., 2001, ApJ, 559, 507
Sharma M., Nath B. B., Chand H., 2013, MNRAS, 431, L93
Shull J. M., Stevans M., Danforth C. W., 2012, ApJ, 752, 162
Silk J., Rees M. J., 1998, A&A, 331, L1
Simcoe R. A. et al., 2013, PASP, 125, 270
Skrutskie M. F. et al., 2006, AJ, 131, 1163
Srianand R., 2000, ApJ, 528, 617
Srianand R., Petitjean P., 2000, A&A, 357, 414
Srianand R., Petitjean P., 2001, A&A, 373, 816
Srianand R., Shankaranarayanan S., 1999, ApJ, 518, 672
Tayal S. S., 2006, ApJS, 166, 634
Tejos N. et al., 2013, MNRAS, 437, 2017
Telfer R. C., Kriss G. A., Zheng W., Davidsen A. F., Green R. F., 1998, ApJ, 509, 132
Tripp T. M., Lu L., Savage B. D., 1996, ApJS, 102, 239
Trump J. R. et al., 2006, ApJS, 165, 1
Veilleux S., Cecil G., Bland-Hawthorn J., 2005, ARA&A, 43, 769
Véron-Cetty M. P., Joly M., Véron P., 2004, A&A, 417, 515
Vivek M., Srianand R., Petitjean P., Noterdaeme P., Mohan V., Mahabal A., Kuriakose V. C., 2012, MNRAS, 423, 2879
Voronov G. S., 1997, Atomic Data and Nuclear Data Tables, 65, 1
Voges W. et al., 1999, A&A, 349, 389
Weymann R. J., Williams R. E., Peterson B. M., Turnshek D. A., 1979, ApJ, 234, 33
Weymann R. J., Morris S. L., Foltz C. B., Hewett P. C., 1991, ApJ, 373, 23
White S. D. M., Frenk C. S., 1991, ApJ, 379, 52
Wild V. et al., 2008, MNRAS, 388, 227
Williams R. E., Strittmatter P. A., Carswell R. F., Craine E. R., 1975, ApJ, 202, 296
Wilms J., Allen A., McCray R., 2000, ApJ, 542, 914
Woo J. H., Urry C. M., 2002, ApJ, 579, 530
Young P. J., Sargent W. L. W., Boksenberg A., Carswell R. F., Whelan J. A. J., 1979, ApJ, 229, 891

APPENDIX A: TIME-DEPENDENT IONIZATION CALCULATIONS

The set of time-dependent ionization equations (equation 31) may be compactly written as

$$\partial_t \boldsymbol{n} = \mathbf{A}\boldsymbol{n}, \tag{A1}$$

where $\boldsymbol{n}$ is a length $N+1$ vector that specifies the ionic number densities for an element with N electrons, and $\mathbf{A}$ is the $(N+1)\times(N+1)$ matrix containing the photoionization, collisional ionization and recombination rate coefficients, derived assuming some temperature,

incident radiation field and electron number density, n_e. These equations are closed by the condition that

$$\sum_{i=0}^{N} n_{M_i} = n_{\rm total}, \tag{A2}$$

where $n_{\rm total}$ can be related to n_e in a highly ionized plasma, assuming solar metallicity and abundances, by

$$n_{\rm total} \approx \frac{2X}{1+X} A_Z n_e. \tag{A3}$$

Here A_Z is the absolute elemental abundance relative to hydrogen and X is the mass fraction in hydrogen. In equilibrium, $\partial_t \boldsymbol{n} = 0$, and we find that

$$\frac{n_{M_{i+1}}}{n_{M_i}} = \frac{\beta_{M_i} n_e + \Gamma_{M_i}}{n_e \alpha_{M_i}} \equiv a_{M_i}. \tag{A4}$$

It is then straightforward to show that we can write any n_{M_i} for $i > 0$ in terms of n_{M_0} via

$$n_{M_i} = \left(\prod_{j=0}^{i-1} a_{M_j} \right) n_{M_0}, \tag{A5}$$

where the scaling factors a_{M_j} are defined above. Therefore,

$$\begin{aligned} n_{\rm total} &= n_{M_0} + \sum_{i=1}^{N} \left(\prod_{j=0}^{i-1} a_{M_j} \right) n_{M_0} = \frac{2X}{1+X} A_Z n_e \\ \Rightarrow n_{M_0} &= \frac{2X A_Z n_e}{(1+X)\left(1 + \sum_{i=1}^{N} \left(\prod_{j=0}^{i-1} a_j \right)\right)}. \end{aligned} \tag{A6}$$

Eliminating n_{M_0}, we finally arrive at an expression that defines the equilibrium number density of some ion n_{M_i} as

$$n_{M_i,{\rm eq}} = \prod_{j=0}^{i-1} a_{M_j} \frac{2X A_Z n_e}{(1+X)\left(1 + \sum_{k=1}^{N} \left(\prod_{j=0}^{k-1} a_{M_j} \right)\right)}, \tag{A7}$$

for $i > 0$.

We first calculate the equilibrium set $n_{M_i,{\rm eq}}$ using equation (A7), assuming $n_e = 10^3\,{\rm cm}^{-3}$ (approximately that inferred from the analysis of Section 4.1) and $X = 0.28$. To examine the effect of changing gas density, we then perturb these values and n_e by a factor $(1+\delta)$. For changes in the incident ionizing flux, we perturb the photoionization rates Γ_{M_i} in an identical fashion. The time-dependent evolution in the number densities, n, of H I, O IV, O V, O VI, Ne VIII and Mg X are then calculated by numerically solving equation (A1), set to initially contain the perturbed $\boldsymbol{n}$ and/or $\mathbf{A}$ (note that both $\boldsymbol{n}$ and $\mathbf{A}$ change if n_e changes). For $\mathbf{A}$, we additionally assume a temperature $T = 10^4$ K and illumination by the 'UV peak' SED at a distance of 2.3 kpc.

In the case of H I, we can obtain an analytical solution to the rate of change in the neutral fraction $x \equiv n_{\rm HI}/n_{\rm H}$, determined by the hydrogen photoionization rate Γ, collisional ionization rate coefficient β, and recombination rate coefficient α, as well as the electron number density n_e, according to

$$\frac{{\rm d}x}{{\rm d}t} = -(\Gamma + \beta n_e) + \alpha n_e (1-x). \tag{A8}$$

For a pure hydrogen gas ($X = 1$), we can express the electron number density as $n_e = (1-x) n_{\rm H}$ and write ${\rm d}x/{\rm d}t$ in the form of a Riccati equation:

$$\frac{{\rm d}x}{{\rm d}t} = R x^2 + Q x + P \tag{A9}$$

$$\begin{aligned} R &\equiv (\beta + \alpha) n_{\rm H} \\ Q &\equiv -(\Gamma + \alpha n_{\rm H} + R) \\ P &\equiv \alpha n_{\rm H} \end{aligned} \tag{A10}$$

(Altay & Theuns 2013). Assuming that P, Q and R are all constant, the time-dependent solution can then be found by separation of variables:

$$x(t) = x_- + (x_0 - x_-) \frac{(x_+ - x_-) F}{(x_+ - x_0) + (x_0 - x_-) F}, \tag{A11}$$

where x_+ and x_- are the roots of the quadratic term in equation (A9), $x_0 \equiv x(t=0)$ is the initial value, and

$$\begin{aligned} F(t) &\equiv \exp\left(\frac{-(x_+ - x_-)\, t}{t_{\rm rec}} \right) \\ t_{\rm rec} &\equiv \frac{1}{(\alpha + \beta) n_{\rm H}}. \end{aligned} \tag{A12}$$

We identify $t_{\rm rec}$ as the recombination time-scale. It can be shown that x_- represents the physical equilibrium solution (Altay & Theuns 2013), so for the density changes described, both $x(t=\infty)$ and $x(t=0)$ take the form of x_-, but with a different value of $n_{\rm H}$. The same applies for incident ionizing flux changes, but with different values of Γ instead.

First, to check the validity of our numerical calculations, we compare the numerically calculated non-equilibrium evolution in the number density of H I for a pure hydrogen gas ($X = 1$) with that computed from equation (A11). We do so for an order of magnitude step function decrease in both the incident ionizing flux and the gas density separately. The results of this comparison are shown in Fig. A1. We find an excellent agreement between these two calculations, which confirms that our numerical results are robust. Full numerical results for the evolution in n following a step function change in density are plotted in Fig. A2 relative to the starting values $n(t=0)$, for a range of values of $(1+\delta)$. A similar calculation for changes in the incident ionizing flux (described in Section 5.2) is presented in Fig. A3. We find that the numerical results in the latter agree well with the typical e-folding time-scales derived in equation (32).

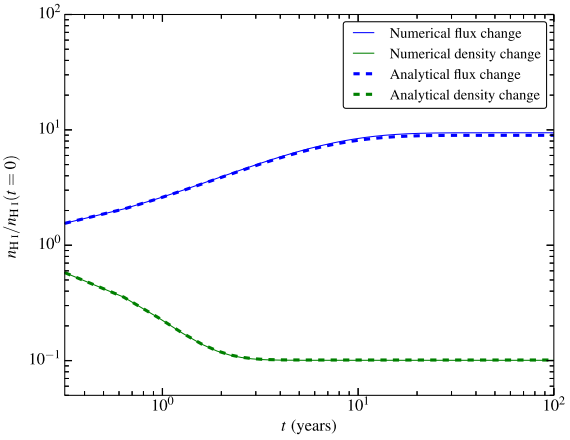

Figure A1. Non-equilibrium evolution in $n_{\rm H\,I}$ following a step function, order of magnitude change in flux (blue) and density (green) in a pure hydrogen gas. Numerical results are shown with solid lines, and analytical results are shown with dashed lines. The results are normalized with respect to the starting value at $t = 0$. We find an excellent agreement between the numerical and analytical calculations.

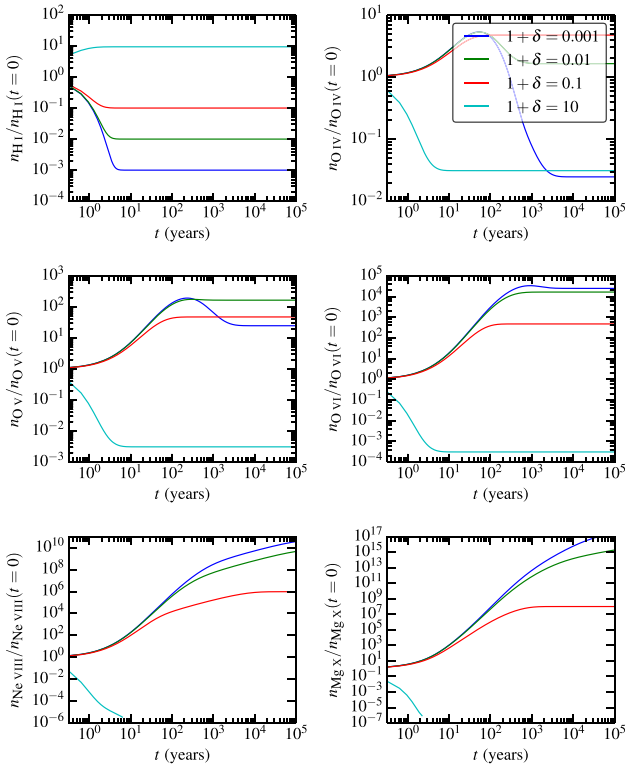

Figure A2. Non-equilibrium evolution in the number density, n, of ions H I, O IV, O V, O VI, Ne VIII and Mg X relative to their starting values, following a step function change in density given by $n(t > 0) = (1 + \delta)n(t = 0)$. We set n at $t = 0$ to the equilibrium values for a temperature $T = 10^4$ K, a distance of 2.3 kpc from the QSO modelled by the 'UV peak' SED, and with $n_{\rm e} = 10^3$ cm^{-3}. Numerical results for a range of $(1 + \delta)$ are presented with different coloured lines. Time-scales for a restored equilibrium are >100 yr for a drop in gas density of more than an order of magnitude, with the exception of H I. Time-scales are orders of magnitude shorter for an increase in gas density.

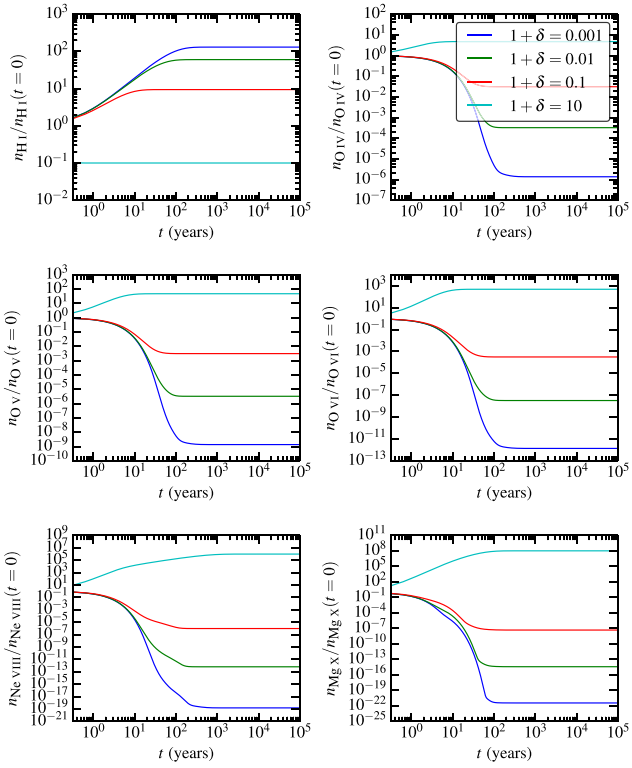

Figure A3. Non-equilibrium evolution in the number density, n, of ions H I, O IV, O V, O VI, Ne VIII and Mg X relative to their starting values, following a step function change in incident flux given by $\Gamma(t > 0) = (1 + \delta)\Gamma(t = 0)$. We set Γ at $t = 0$ to the photoionization rate at a distance of 2.3 kpc from the QSO modelled by the 'UV peak' SED. Numerical results for a range of $(1 + \delta)$ are presented with different coloured lines. Time-scales for a restored equilibrium are, typically, <100 yr. These results agree well with the typical e-folding time-scales derived in equation (32).

This paper has been typeset from a TEX/LATEX file prepared by the author.